Koh et al. *Microsystems & Nanoengineering* (2026)12:16
https://doi.org/10.1038/s41378-025-01128-6

Microsystems & Nanoengineering
www.nature.com/micronano

REVIEW ARTICLE Open Access

Electrostatically actuated MEMS resonators for magnetic and electric field sensing: a review

Daeyeon Koh[1], Yohan Jung[1] and Jongbaeg Kim[1]✉

Abstract
Recent advances in microelectromechanical systems (MEMS) resonators have enabled the development of compact devices capable of precise magnetic and electric field sensing. This review focuses on resonant MEMS sensors that employ electrostatic actuation, offering advantages such as low power consumption, fast mechanical response, and CMOS-compatible fabrication. We classify two primary types of resonant MEMS sensors based on their sensing mechanisms, where magnetic field sensors utilize electromagnetic induction and electric field sensors rely on electrostatic induction. For each type, we analyze representative devices in terms of actuation schemes, resonator design strategies, sensitivity enhancement techniques, and directional detection capability. We also address key design considerations and fabrication constraints. The review summarizes current approaches and characteristics of MEMS resonator-based magnetic and electric field sensors with a focus on their structural principles and application contexts. Through this analysis, the review aims to provide insights that support the development of next-generation field sensors for applications in navigation, biomedical diagnostics, vehicle detection, and non-destructive evaluation of electrical systems.

Introduction

A microelectromechanical system (MEMS) is a micrometer-scale transducer that integrates microstructures and electrical circuits[1,2]. MEMS devices offer advantages due to their small size, various energy conversion principles, and integrated circuit (IC) compatibility. The development of durable micromachining tools and packaging technologies has enhanced the recognition of MEMS in the modern electronics industry, enabling their applications across various industrial fields[3–6]. Because of the diversity of applicable energy conversion schemes, MEMS sensors are widely employed to detect a range of chemical, mechanical, and electrical properties. Compared to macroscale sensors, MEMS sensors provide reduced size and weight, compatibility with other systems, and low manufacturing cost through batch fabrication. In terms of sensing performance, MEMS sensors offer high reliability, fast response, and high sensing resolution. These characteristics of MEMS devices make them excellent candidates for detecting magnetic and electric fields[2–4].

MEMS magnetic field sensors based on electromagnetic induction measure the induced voltage generated by changes in the effective area of the induction coil within a magnetic field. MEMS electric field sensors utilizing electrostatic induction measure electric fields by converting current, induced by charge changes in sensing electrodes under electric fields, into voltage. Both magnetic and electric field sensing mechanisms require the movable components of MEMS sensors to generate repeated, large mechanical displacements for effective operation. Therefore, the integration of resonators is crucial for the functionality of these sensors. Typical resonant driving methods for MEMS include electrothermal, electromagnetic, piezoelectric, and electrostatic actuation, each with its own advantages and disadvantages[5,6]. The selection among these methods depends on the design objectives and operating conditions.

Electrostatic forces arise from attractive or repulsive interactions between charged conductors and are widely exploited as an effective actuation mechanism in MEMS due to their low power consumption, high-speed

---

Correspondence: Jongbaeg Kim (kimjb@yonsei.ac.kr)
[1]School of Mechanical Engineering, Yonsei University, 50 Yonsei-ro, Seodaemun-gu, Seoul 03722, Republic of Korea
These authors contributed equally: Daeyeon Koh, Yohan Jung

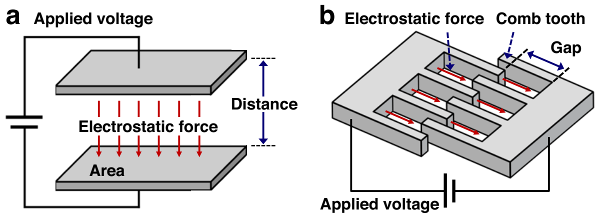

Fig. 1 Schematic illustration of typical MEMS electrostatic actuators. a An actuator driven by the electrostatic force between two parallel plates. **b** A comb-drive actuator with interdigitated teeth. The electrostatic force of the comb drive is not affected by the distance between the two electrodes. Thus, the comb drive is conveniently controllable

response, and compatibility with standard microfabrication processes. Electrostatic MEMS actuators are typically classified into two main categories: gap-closing actuators and comb-drive actuators, as illustrated in Fig. 1.

Gap-closing actuators generate motion by applying a voltage between two parallel electrodes, generating electrostatic force that draws the electrodes toward each other, as shown in Fig. 1a[7–9]. The resulting actuation is inherently nonlinear, as the electrostatic force increases sharply with decreasing gap distance. This nonlinearity leads to a pull-in instability, which limits the maximum stable displacement and compromises device reliability[7]. As a result, the operational range of gap-closing actuators is constrained, making them less suitable for applications that require large or precisely controllable displacements.

To address these limitations, comb-drive actuators have been developed[10–13]. Comb-drive actuators, as presented schematically in Fig. 1b, consist of interdigitated finger-like electrodes arranged laterally. Unlike gap-closing structures, the electrostatic force in comb drives is largely independent of displacement and is instead governed by the geometry of the comb structure, including finger width, overlap length, and gap spacing. This results in a nearly constant and linear force over the range of motion, which in turn facilitates precise displacement control with high resolution and enhanced operational stability. Moreover, the comb-drive architecture can be efficiently fabricated using standard planar micromachining techniques, offering advantages in scalability and IC-compatibility[14]. Due to these benefits, comb-drive actuators have been widely adopted in various MEMS applications, including resonators, inertial sensors, micro-mirrors, and optical scanning systems.

Electrostatic MEMS actuators offer key advantages such as low power consumption, fast response time, and compatibility with standard microfabrication processes. Although they often require relatively high driving voltages to achieve large displacement for resonance operation, the absence of current flow across the dielectric gap allows for extremely low power consumption compared to other actuation methods. The simplicity of their structural design also facilitates easy integration with ICs, making them highly attractive for compact and scalable MEMS systems. Given that gap-closing actuators offer compactness but are constrained by pull-in effects, and comb-drive actuators provide broader design flexibility with improved stability and resolution, careful selection between the two is essential depending on specific design goals and operational environments. Building upon these foundational characteristics, this review focuses on MEMS sensors that detect magnetic and electric fields by applying electrostatic resonance actuation. Additionally, we also discuss their potential applications and highlight the challenges that remain to be addressed.

Electrostatic actuation for MEMS resonators

Electrostatic actuation is one of the most prevalent driving schemes for MEMS resonators, offering simplicity, scalability, and compatibility with standard microfabrication processes[15]. Because the generated electrostatic force depends nonlinearly on both the applied voltage and electrode displacement, such systems inherently exhibit complex dynamic behaviors that govern the resonance stability and sensing performance[16,17]. Stable and reliable operation requires precise driving and control schemes capable of maintaining consistent resonance amplitude and phase under variations in temperature, humidity, and other environmental disturbances[18]. In this section, we discuss the nonlinear dynamics governing electrostatically actuated MEMS resonators and introduce the open-loop and closed-loop control schemes including self-oscillation and phase-locked loop (PLL) that ensure long-term frequency and amplitude stability as well as signal-to-noise ratio (SNR) enhancement in resonator-based sensors.

Nonlinear dynamics in electrostatic resonators

Electrostatic actuation can induce nonlinear dynamic effects in MEMS resonators, and the extent of these effects depends on actuator geometry and operating conditions[19,20]. Because the capacitance varies inversely with the electrode gap in parallel-plate configurations, the electrostatic force increases nonlinearly with displacement[21]. This quadratic voltage dependence leads to electrostatic softening and pull-in instability, while geometric nonlinearities in the mechanical stiffness can counteract this effect, producing either overall softening or hardening behavior depending on the design. In contrast, comb-drive actuators are designed so that the overlap area between interdigitated fingers changes nearly linearly with lateral motion, yielding an approximately constant force for small displacements. However, under torsional oscillation or unintended rotational coupling, even comb-drive resonators can exhibit amplitude-dependent resonance shifts and effective stiffness variations, leading to either softening or hardening behavior depending on structural symmetry and operating conditions[22,23]. When the applied voltage becomes sufficiently large, the effective stiffness decreases due to electrostatic softening, causing resonance-frequency shifts and potential pull-in collapse when the attractive force exceeds the restoring force[24].

In multi-degree-of-freedom MEMS devices such as gyroscopes, accelerometers, magnetometers, and micromirrors, coupling between vibration modes introduces additional nonlinear effects, often resulting in amplitude imbalance, resonance detuning, and degraded dynamic stability[25]. To mitigate these nonlinearities, various modeling and compensation approaches have been explored. The electrostatic force is often linearized near small-displacement regions to simplify analytical modeling, although this approximation becomes inaccurate at large oscillation amplitudes where nonlinear stiffness effects dominate[26]. Conventional proportional–integral–derivative (PID) control remains effective for maintaining amplitude stability and suppressing small disturbances within moderate operating ranges[27]. However, because PID control relies on linear feedback, its ability to compensate for amplitude–phase coupling and parameter drift arising from electrostatic softening is inherently limited, particularly under varying bias voltages or environmental conditions[28]. Consequently, more advanced compensation strategies and adaptive or learning-based frameworks have been explored to enhance robustness against these nonlinearities[29–31].

Recent developments have applied fuzzy-learning and neural-network-assisted controllers to vibratory gyroscopes, enabling real-time adaptation to time-varying parameters while compensating for modeling uncertainties. Xu et al.[32] proposed an intermittently dynamic fuzzy learning-based tracking control (IDFL-TC) that dynamically recruits or prunes neurons and intermittently updates learning weights, effectively balancing tracking precision and computational efficiency. Similarly, asynchronous tracking-control (ATC) schemes have demonstrated amplitude stability under partially unknown mode information through adaptive feedback and fuzzy-learning mechanisms[33]. These data-driven control frameworks substantially enhance robustness and adaptability, providing precise resonance regulation in electrostatically driven MEMS resonators under nonlinear and uncertain operating conditions.

Electrostatic driving control system

For reliable electrostatic operation, MEMS resonators can be driven in open-loop for characterization and simple readout, but precision sensing typically requires closed-loop control to stabilize frequency, amplitude, and phase[24,34]. Figure 2 summarizes the control architectures of MEMS electrostatic resonator-based sensors: open-loop and closed-loop scheme. Representative closed-loop strategies include self-oscillation loops and phase-locked loops that mitigate thermal and bias drift over time. In block diagram terms, both open- and closed-loop implementations comprise drive generation, the resonator, sensing electrodes, amplification and phase detection, loop filtering, and bias generation stages.

Open-loop operation

Figure 2a shows a block diagram of open-loop control system of resonant MEMS sensors. In open-loop operation, the resonator is driven with a prescribed tone and its response is read out without feedback. This mode is simple, enables rapid frequency sweeps for modal

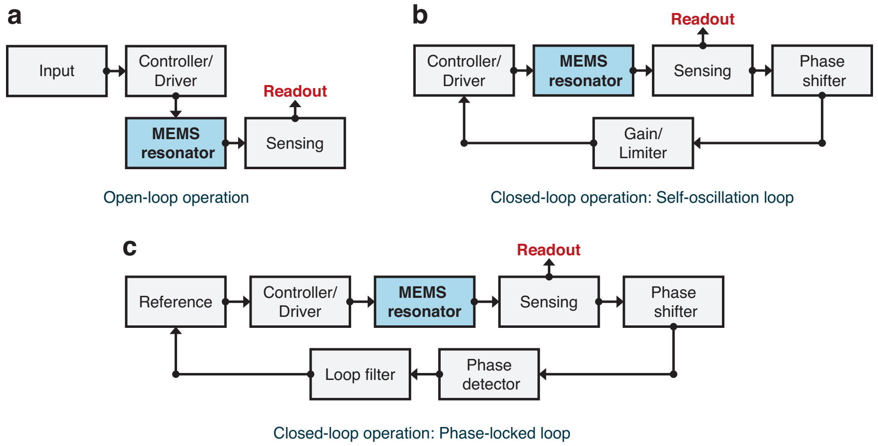

Fig. 2 Block diagrams for control schemes of electrostatic resonance MEMS sensors. a In an open-loop system the user modulates the input with no feedback. **b** The self-oscillation system, one of a closed-loop scheme, uses feedback control to satisfy the Barkhausen condition. **c** The PLL is a closed-loop system that measures phase error and adjusts the drive frequency to keep quadrature

identification and calibration, and is often used to extract small-signal parameters such as quality factor (Q-factor), motional impedance, and electrostatic gain. The main limitation is sensitivity to drift in both frequency and amplitude. Slow variations in temperature, bias voltage, and ambient pressure, together with intrinsic thermoelastic effects, shift the resonance peak and modify the mechanical gain, which directly perturbs the demodulated output in field-sensing use cases[35–37].

Closed-loop operation

As mentioned above, in electrostatic MEMS resonators, the resonance frequency and scale factor vary with the ambient environment and the drive conditions. Temperature perturbs the device through thermoelastic mechanisms and through packaging effects such as cavity pressure and gas viscosity that modify damping and effective stiffness[36]. The apparent spring constant also softens with applied bias, so slow drift in the bias or supply translates into frequency and gain drift. To actively compensate these effects, closed-loop architectures regulate one or more resonator state variables to suppress drift and linearize transduction.

A self-oscillation loop sets phase and gain to satisfy the Barkhausen condition so the device oscillates at its natural resonance without a separate timing reference[38], as illustrated in Fig. 2b. As the environment changes, the oscillation frequency follows the resonant shift, which makes implementation simple and power efficient but ties stability to the resonator's own drift. A PLL system, as shown in Fig. 2c, locks an internal numerically controlled oscillator to the resonator's phase condition so the drive stays in quadrature[39]. The sensed phase passes through a loop filter to adjust the drive frequency; proper capture and hold-in ranges, loop bandwidth, and phase margin track slow thermal or bias shifts while rejecting high-frequency noise and avoiding peaking. In high-Q shell resonators, nested digital loops for frequency, amplitude, and quadrature reduce inter-loop coupling and improve long-term stability, and the same structure applies to electrostatically driven field-sensing MEMS[40].

In closed-loop operation, amplitude regulation stabilizes the scale factor and keeps motion in the linear range, reducing pull-in or compression risk. Automatic gain control (AGC) alongside self-oscillation or a PLL holds a constant amplitude for linear amplitude-readout sensitivity by comparing the envelope to a setpoint and adjusting drive gain[38]. The AGC response should be slower than the resonator's amplitude dynamics and the frequency-tracking bandwidth to avoid amplitude–phase coupling and noise peaking; with proper setpoints it prevents front-end saturation and can improve SNR, while frequency-output sensitivity is primarily set by the frequency-tracking loop. In addition, adding thermal-drift[41] and bias-drift[42] models on top of AGC and frequency tracking system provides feedforward correction and reduces residual drift beyond what feedback alone can achieve.

Signal-to-noise ratio enhancement for MEMS sensors

In resonator-based MEMS sensors, where the mechanical resonance of microstructures is transduced into electrical signals through various coupling mechanisms, the SNR, defined as the ratio between signal strength and noise level, determines the achievable resolution and minimum detectable signal[43]. As device dimensions continue to shrink, compliant mechanical structures become more susceptible to both intrinsic and extrinsic disturbances, leading to smaller transduced electrical outputs. Consequently, the signal can be buried beneath the noise floor, and the total noise originating from thermomechanical, electronic, and flicker sources collectively define the ultimate sensitivity limit. The total noise floor originates from multiple physical mechanisms, including intrinsic thermomechanical noise, electronic noise from the readout circuitry, and low-frequency flicker noise[44,45]. These noise components collectively define the ultimate sensitivity limit of the device, particularly under weak-field conditions in external field sensing or during low-amplitude operation. A detailed understanding of these noise sources is therefore essential for improving the overall detection performance of resonant MEMS sensors.

The noise processes that influence resonant MEMS sensors originate from both mechanical and electrical domains. Thermomechanical noise, originating from the intrinsic energy dissipation and Brownian motion of the resonator, defines the fundamental mechanical limit of sensitivity[46]. Its magnitude is governed by the damping level and ambient temperature, as described by the fluctuation–dissipation theorem[47]. Electronic noise, which includes Johnson–Nyquist thermal noise from resistive elements, shot noise in bias circuits, and amplifier input noise, arises from the readout and drive electronics[48]. These components dominate the high-frequency region of the spectrum and can obscure weak resonant signals, particularly when the electromechanical transduction efficiency is low. Flicker noise (1/f noise) becomes significant in the low-frequency regime[49,50]. Although primarily associated with semiconductor interfaces, it can also manifest in resonant MEMS devices through slow potential fluctuations along conductive paths such as doped silicon regions, metallic electrodes, and interconnecting wires. These fluctuations lead to baseline drift and offset instability. Since these noise sources originate from both the mechanical and electronic domains, effective noise suppression requires comprehensive optimization of the device structure, transduction scheme, and circuit design to minimize the overall noise floor.

Enhancing the SNR requires concurrent optimization of the mechanical structure, electrical readout, and system-level control. Mechanically, improving the Q-factor through symmetric structural design, low-loss materials, and reduced air damping decreases the equivalent thermal force noise and narrows the resonance bandwidth, thereby reducing the overall displacement noise floor within the sensing bandwidth[51,52]. Electrically, employing low-noise amplifiers, differential or chopper-stabilized readout architectures, and proper grounding and shielding minimizes the voltage and current noise contributions from the readout chain[53,54]. At the system level, closed-loop amplitude control maintains constant vibration amplitude under varying environmental conditions, while quadrature compensation suppresses phase errors and mitigates parasitic coupling between drive and sense modes. For example, modeling studies on fully closed-loop resonant systems, such as hemispherical resonator gyroscopes under force-to-rebalance operation, have shown that dynamic coupling analysis of driving and detecting loops can effectively suppress interference-induced output errors and maintain stable amplitude tracking[55].

By integrating these strategies, resonant MEMS sensors can approach their fundamental noise limits, achieving enhanced SNR and improved resolution even under ambient or weak-field conditions in field-sensing applications. However, higher resolution does not always imply better performance, as it inherently involves trade-offs among sensitivity, bandwidth, accuracy, and response speed, as well as between performance, power consumption, and circuit complexity[56,57]. Achieving extremely high resolution often demands low-noise electronics, high-resolution analog-to-digital converters (ADCs), and increased power consumption, which together impose greater system complexity and data processing requirements[58]. Therefore, an optimal resolution should be determined according to the target application, balancing sensitivity, noise performance, and practical constraints. Maintaining this balance is crucial for realizing reliable, energy-efficient, and scalable MEMS sensing systems that can operate effectively in real-world environments.

Magnetic field sensors

Magnetic field sensors, which measure the strength and direction of an external magnetic field, are used in various industrial fields, including position sensing, archaeology, the automotive industry, the medical industry, space research, brain mapping, navigation, and non-destructive diagnosis, depending on their sensing range and resolution[59–62]. Existing technologies for magnetic field detection include Hall sensors, search coils, superconducting quantum interference devices (SQUIDs), fluxgate sensors, anisotropic magnetoresistive (AMR) and giant magnetoresistive (GMR) sensors, as well as MEMS-based magnetic field sensors[63,64]. MEMS magnetic field sensors offer advantages such as small form factor, fast response, and batch-process compatibility. A widely studied category of MEMS magnetic sensors is based on Lorentz force transduction, where an electrical current flowing through a microstructure interacts with an external magnetic field to generate a Lorentz force[65,66]. This force induces displacement and a shift in the resonant frequency of the vibrating structure, which are measured using various transduction methods, including piezoelectric[67–71], capacitive[72–74], piezoresistive[75–77], and optical techniques[78–81].

Two representative signal transduction methods in Lorentz-force-based MEMS sensors are amplitude modulation (AM) and frequency modulation (FM). In AM-type sensors, the magnetic field–induced Lorentz force modulates the amplitude of vibration. While straightforward in implementation, this approach often suffers from low SNR under small magnetic fields. In contrast, FM-type sensors rely on resonators driven by comb drives, where the Lorentz force introduces an axial load that shifts the resonant frequency. The external magnetic field strength is inferred from the resulting frequency shift, typically measured by sensing comb capacitors[82–86]. Techniques such as mechanical leverage can amplify this frequency shift and significantly enhance sensitivity. An improvement of up to 42 times has been reported compared to unamplified designs[86].

Despite their utility, Lorentz-force-based MEMS sensors face intrinsic challenges. High excitation currents are typically required to generate measurable displacements or frequency shifts, which increases power consumption and induces Joule heating. This can lead to thermal stress, drift, and mechanical instability in the resonator[87]. Furthermore, the current-carrying structures require complex electrical routing and readout circuits, which may limit integration density and reliability. To address these limitations, recent studies have explored alternative MEMS magnetic field sensing schemes that decouple actuation and sensing mechanisms. In particular, sensors that combine electrostatic actuation with electromagnetic induction sensing have gained attention as a low-power and thermally stable alternative.

Electrostatically driven MEMS magnetic field sensor using electromagnetic induction

Several recent studies have proposed MEMS magnetic field sensors that use electrostatic actuation and electromagnetic induction sensing[87–95]. The MEMS sensors driven by electrostatic force have the advantage of low power consumption without self-heating compared with being driven by the Lorentz force. Also, electromagnetic induction sensing provides a direct voltage output, which simplifies the readout circuitry, and inherently exhibits excellent linearity to the applied magnetic field. MEMS magnetic field sensors based on electrostatic force driving and electromagnetic induction sensing have the following advantages over other magnetic field sensing methods. First, a search coil measures only time-varying magnetic fields, whereas electromagnetic induction sensing technology can theoretically detect static and alternating magnetic fields[88]. Second, unlike magnetoresistive sensors, this technology is free from magnetic hysteresis, as it does not require a unique magnetic material[89]. Third, the manufacturing processes of MEMS magnetic field sensors are simpler than the complicated production of fluxgate sensors that require the magnetic core and coil to be integrated[65]. Although the resolution is not higher than that of SQUID, the advantages of MEMS magnetic field sensors are their low power consumption and low cost[87].

Figure 3a, b shows schematic diagrams of the sensing mechanism using electrostatic driving and electromagnetic induction sensing for out-of-plane and in-plane magnetic fields, respectively. The area covered by the induction coil within the magnetic field changes by the in-plane[87–91] or torsional[92–95] motion of the structure. The structure is moved with electrostatic driving by comb drives or parallel plates. Changes in the induction coil area result in changes in the magnetic flux passing through the induction coil, and an induced electromotive force is generated by the electromagnetic induction principle. Liu et al.[87] presented an analytical model of a resonant MEMS magnetic field sensor using electromagnetic induction sensing. The following equation expresses the induced electromotive force (ψ) of the single induction coil in a static magnetic field.

$$\psi = B\frac{dS}{dt} \tag{1}$$

where B is the magnetic flux density, S is the area covered by the induction coil, and t is the time. As the area covered by the single induction coil changes, the magnetic flux changes, resulting in an induced electromotive force. The following equation expresses the sensitivity (U) of the magnetic field sensor:

$$U = \frac{\partial|\psi|}{\partial B} \tag{2}$$

Device modeling can theoretically obtain the sensitivity of an electromagnetic induction-based magnetic field sensor. Because the vibration amplitude of the patterned induction coil on the resonant plate is the same as that of the resonant plate, it can be determined by employing the second-order differential equation of the motion of the resonant plate using the Laplace transform. The induced electromotive force generated in a single induction coil is calculated using the change in the coil area as a function of time from the vibration amplitude of the resonant plate. The induced electromotive force generated in every induction coil is independent, and the total output voltage is obtained by summing the voltages induced in all the coils. Therefore, the sensitivity of the magnetic field sensor can be obtained by dividing the summed induced voltage

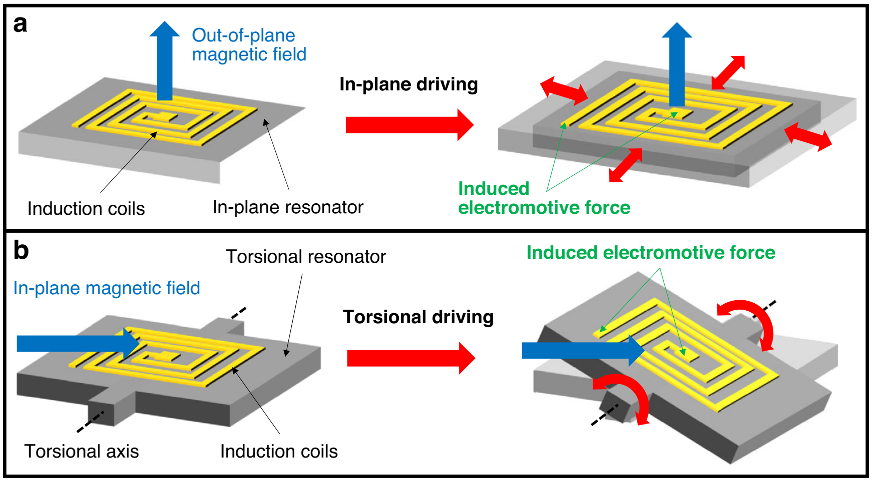

Fig. 3 Schematic diagram of the magnetic field sensing mechanism based on electrostatic actuation and electromagnetic induction. a For in-plane driving, the out-of-plane magnetic field passes through the area enclosed by the coil, which changes due to the lateral motion of the structure. **b** For torsional driving, the in-plane magnetic field passes through the coil area, which changes as the structure rotates. In both cases, the effective magnetic flux through the coil varies with time, generating an electromotive force via electromagnetic induction

by the applied magnetic field strength. To enhance sensitivity, it is essential to increase the induced electromotive force, which is proportional to the rate of change of magnetic flux. Because magnetic flux depends on both the area and motion of the coil, sensitivity can be improved by increasing the displacement amplitude and vibration frequency of the resonator. A higher driving voltage strengthens the electrostatic force, resulting in larger resonator displacement and thus greater flux variation. Operating in vacuum reduces air damping, which increases the oscillation amplitude and Q-factor, further increasing the induced voltage. Higher resonant frequency accelerates the flux change rate, leading to stronger output signals. Additionally, increasing the number of coil turns proportionally raises the total induced voltage, thereby enhancing sensitivity. Coil geometry optimization, including turn count and spacing, is also critical to maximize performance while ensuring structural integrity.

Out-of-plane MEMS magnetic field sensing

Wu et al.[89] proposed a novel out-of-plane MEMS magnetic field sensor for capacitive driving and electromagnetic induction sensing. Figure 4a shows a schematic of the sensor configuration. The sensor consists of a square plate resonator that contracts and extends symmetrically on four sides, with planar induction coils on its upper surface. The ends of the induction coil were formed outside the resonant plate using the second electrical isolation layer and the second metal layer. The device was fabricated using a cavity-silicon-on-insulator process. In the square extensional (SE) mode, all four sides of the resonant plate contract and extend in phase. The induced electromotive force generated from each part of the induction coil on the resonant plate is summed to detect the output signal.

The Q-factor is a physical quantity representing the resonance characteristics. A high Q-factor indicates less energy loss per oscillation cycle relative to the stored energy of the resonator. This resonant characteristic affects the sensitivity and resolution of the sensor by determining the amplitude of vibration at resonance and the sharpness of the frequency response. A higher Q-factor results in larger vibration amplitudes and a narrower bandwidth. In electromagnetic induction sensing, the induced voltage is proportional to the rate of change of magnetic flux through the coil. Since a higher Q-factor yields greater vibrational amplitude at resonance, it produces larger flux variations, thereby enhancing the induced voltage and improving the sensitivity and resolution of the sensor. Compared with the Q-factor of the SE mode resonator without coils, the Q-factor of the coil-integrated magnetic field sensor is reduced from 6000 to 3700 owing to the energy loss caused by the additional mass, such as the oxide layer and the metal layer. The amplitude–frequency response of the sensor was measured in 60 mT steps under ambient atmospheric conditions, over the range of 20–320 mT. The sensor has good linearity and sensitivity of 3 μV/mT. The authors reported analytic modeling to optimize the design of the same structure[87]. Within design constraints such as the device size and minimum line width resulting from the manufacturing process, the structural parameters such as the length of the resonant plate, length of the driving electrode, width, turn, and spacing of the induction coil were optimized for enhanced sensitivity.

Wu et al.[90] presented a method to improve the resonance characteristics such as the Q-factor and sensitivity of magnetic field sensors by utilizing vacuum packaging and mechanically coupled a dual resonator design. Figure 4b presents a schematic of the coupled dual resonator vibrating in the SE mode along with the mode shape obtained by finite element simulation (COMSOL Multiphysics). The dual resonator array increases the induced electromotive force because of the summation of outputs generated from individual resonators and has the effect of boosting the Q-factor. Compared with the previously reported sensor[89], the sensitivity of the magnetic field sensor, with a sensitivity of 3 μV/mT in single SE resonating mode, is increased by more than 10 times. Also, vacuum packaging prevents considerable energy dissipation owing to air damping. The SEM image shows the fabricated device before vacuum packaging. The chip-level packaging process entailed eutectic bonding and wire bonding with the magnetic field sensor and ceramic chip. Afterward, the vacuum sealing process was carried out in a high-vacuum furnace with the pressure lowered to 10^{-6} Torr, and the lid with the getter material was subjected to eutectic bonding. As a result of the vacuum-packaging, the energy dissipation caused by air damping is lowered, thereby increasing the sensitivity and also the Q-factor to 42,000, which is more than 10 times higher than the Q-factor of ~4000 in air. Besides, the vacuum-packaged sensor resonates at a frequency of 4.319 MHz with a sensitivity of 35.92 μV/mT and 47.74 μV/mT, and linearity errors of 0.65% and 1.19% at driving voltages of DC 30 V and 40 V, respectively. As the driving DC bias increased from 30 V to 40 V, the sensitivity increased by more than 1.3 times because of the increased vibration amplitude and velocity of the coil-integrated SE mode resonator.

Zhang et al.[91] fabricated an electromagnetic induction-based MEMS magnetic field sensor by using silicon-on-insulator multi-user micro-electromechanical system (MEMS) processes using three photomasks. As shown in Fig. 4c, the sensor is composed of one U-shaped gold induction coil on a pair of clamped-clamped beams using simple fabrication processes without an electrical insulation layer. The U-shaped induction coil resonates with the

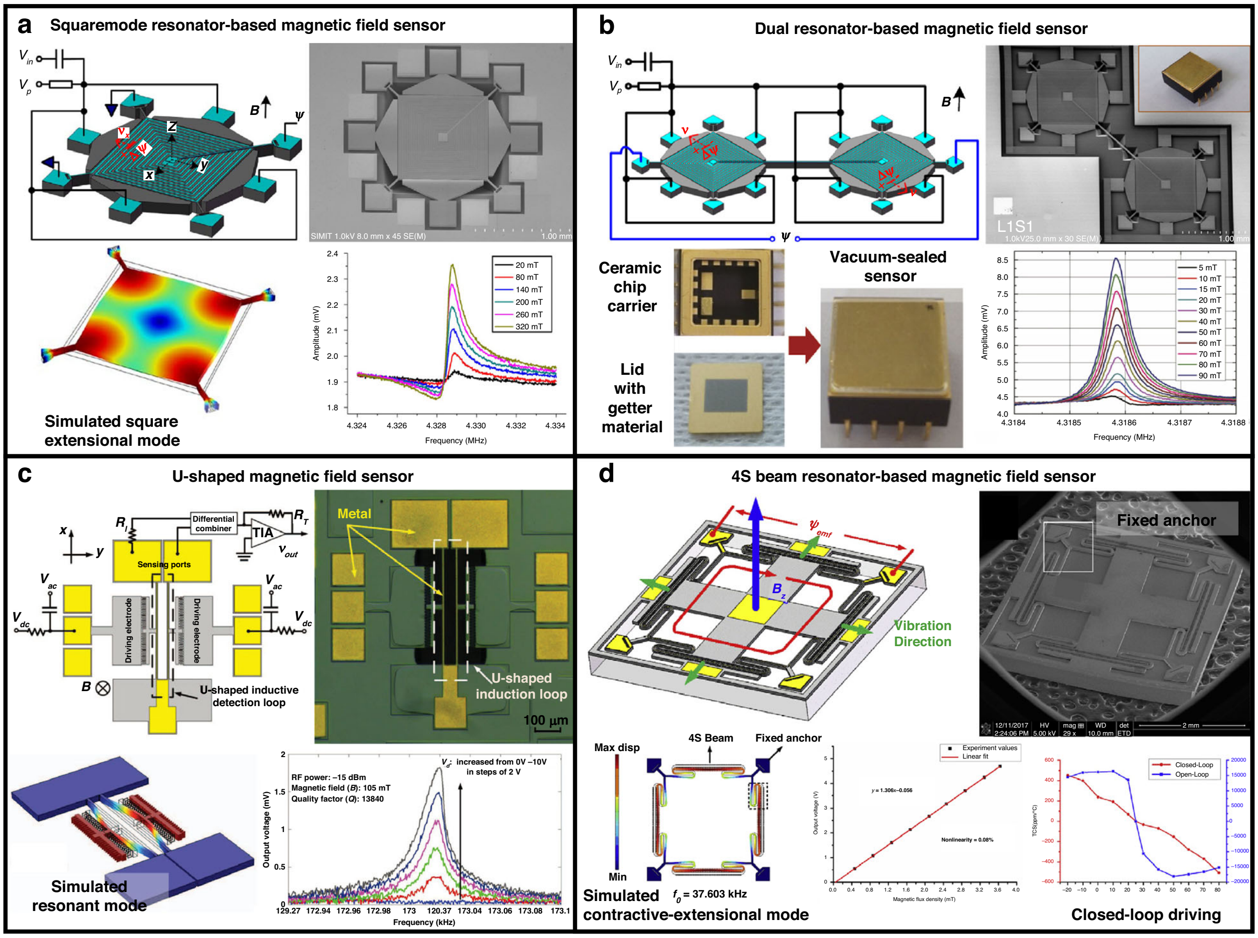

Fig. 4 Out-of-plane MEMS magnetic field sensors driven by electrostatic force. a Square extensional mode resonator-based magnetic field sensor[89]. Schematic diagram of a sensor symmetrically resonantly driven by four driving electrodes and its measured frequency response in 60 mT steps (20–320 mT). The induced electromotive force increased linearly with the applied magnetic field. **b** Dual resonator-based magnetic field sensor[90]. Schematic diagram of a mechanically coupled dual-micro resonator design and mode shape obtained by finite element method (FEM) simulation. SEM image of a cavity-SOI fabricated sensor and optical image of a vacuum-packaged device. **c** Double-ended tuning fork (U-shaped) resonator-based magnetic field sensor[91]. Schematic diagram of a differential readout circuit with a single U-shaped induction coil and measured frequency response at 105 mT under DC voltage actuation (0–10 V, 2 V steps). **d** 4S beam resonator-based magnetic field sensor[88]. Schematic diagram showing two S-shaped folded beams and a long beam with symmetrically distributed comb drives. SEM images of the fabricated structure with two-layer coil connection, and frequency response under closed-loop driving

comb drive attached to both beams. The stiff and bulky SE mode resonator, described in a previous paper[89], was fabricated in complex processes requiring six photolithography steps. And, the fabrication method unavoidably requires the deposition and patterning of an insulation oxide interlayer. Although the advantage of the bulk mode is that the influence of air damping on the Q-factor is small, the sensitivity decreases because of the increased stiffness of the resonator. Because the sensor with the structure of a double-ended tuning fork has flexural beams, the excitation voltage was lowered to 5 V, and the sensitivity was increased to 17.7 mV/T. The measured voltage frequency response shows the increase in the induced electromotive force when the DC driving voltage is increased in steps of 2 V in the range 0−10 V at a constant magnetic field strength of 105 mT. The improvement in sensitivity is attributable to the increase in the vibration amplitude as the driving voltage increases. In terms of the sensing accuracy, parasitic feed-through and capacitive motional currents, which cause undesirable offsets in the output, were effectively removed using a differential readout scheme.

As shown in Fig. 4d, Liu et al.[88] proposed an out-of-plane magnetic field sensor featuring a 4S beam resonator with 12 turns of two-layer induction coils. The 4S beam resonator has four oscillation elements consisting of two S-shaped folded beams and a long beam. Their magnetic field sensor has a large displacement due to the flexure spring and a large size of $4000 \times 4000\ \mu m^2$. This design improvement increased the sensitivity (1306 mV/μT) of the magnetic field sensor by more than 73 times compared to that of Zhang et al.[91]. The driving and sensing combs are distributed symmetrically on both sides of the long beam. With the comb drive excited by an electrostatic force, the 4S beam structure vibrates in the contractive-extensional mode at the resonance frequency. An induced electromotive force is generated by the induction coil laid on the structure. An interface circuit with closed-loop self-oscillation was also constructed using the motional current detected from the sensing comb. The mechanical resonance frequency of the resonator is affected by variations in temperature. Therefore, a slight deviation from the drive frequency and a change in the air viscosity caused by the temperature dramatically decrease the sensitivity of the sensor, which is composed of a resonator. Temperature-independent sensitivity would require an interface circuit to be connected to the sensor. The two-layer coils are electrically connected through a common port, insulated by an electrical isolation layer between them, and placed in the same winding direction. This sensor operates at a resonant frequency of 37.63 kHz in air. The sensor has excellent linearity, a linearity error of 0.08%, a Q-factor of 517, and a resolution of 2.57 μT at AC 1.5 V_p and DC 25 V.

In-plane MEMS magnetic field sensing

Detection of the total magnetic field strength and direction requires accurate magnetic field component measurement. Therefore, it is necessary to measure the in-plane as well as the out-of-plane magnetic field. Liu et al.[92] proposed an electromagnetic induction-based MEMS magnetic field sensor in a torsional mode for in-plane magnetic field sensing. As shown in Fig. 5a, the seesaw plate ($2000 \times 2000 \times 50\ \mu m^3$) fabricated by the standard silicon-on-glass process consists of two torsional beams and two layers of aluminum induction coils. Two equivalent parallel-plate driving electrodes electrostatically vibrate torsional motion at a distance of 2.4 μm. When an in-plane magnetic field is applied, the induction coils on the torsionally driven seesaw plate cut the magnetic induction line. The principle of electromagnetic induction generates an induced voltage. The SEM image shows induction coils and the damping holes formed on the seesaw plate. The damping holes ($100 \times 10 \times 52.4\ \mu m^3$) increase the sensitivity because they reduce the vibrational degradation caused by air damping. Operation of this sensor in air resulted in a sensitivity of 100 mV/mT, a linearity error of less than 0.3%, a high resolution of 25 μT, and low power consumption of less than one microwatt. As the pressure in the experiment decreases, the sensitivity increases rapidly. At 500 Pa pressure, the sensitivity and resolution increased by 41 times and 0.6 μT, respectively, compared with air conditions.

As shown in Fig. 5b, Liang et al.[93] proposed a torsional MEMS magnetic field sensor based on electromagnetic induction using vertically interlaced combs for in-plane magnetic field sensing. The vertically interlaced comb drive, in which fixed and movable comb fingers are alternately arranged on different vertical layers rather than in a single plane, increases the effective actuation area without enlarging the footprint. This configuration also significantly reduces air damping by enabling more efficient airflow between the comb fingers under atmospheric pressure. As a result, both the sensitivity and Q-factor are greatly enhanced. Compared with the performance of the in-plane magnetic field sensor equipped with a parallel-plate electrostatic drive[92], the sensitivity of the sensor with the comb-shaped drive increased by 4.9 times and the Q-factor by 81 times at atmospheric pressure. The sensitivity and Q-factor of the former is 100 mV/mT and ~5.3, respectively, whereas the corresponding properties of the latter are 491 mV/mT and ~430, respectively. For accurate three-axis magnetic field sensing, it is essential to minimize cross-interference. The sensor exhibited an X-axis sensitivity of 491 mV/mT, while the sensitivities along the Y- and Z-axes were 4 mV/mT and 7 mV/mT, respectively. The significant difference in the sensitivity of each of these axes indicates low cross-interference. The magnetic field sensor operating at atmospheric pressure shows a linearity error of less than 0.4%, high resolution of 6 μT, and ultralow consumption of 75 nW.

The resonance characteristics of the MEMS magnetic field sensor were also evaluated using electrostatic detection, but this method introduced errors in the resonance frequency and Q-factor measurements due to feed-through effects. A Lorentz fit was therefore applied to obtain the amplitude-frequency response without the appearance of an anti-resonant peak. By contrast, electromagnetic detection allowed the amplitude-frequency response to be measured without feed-through, enabling a more accurate determination of the resonance characteristics. Since the electromagnetic induction-type magnetic field sensor operates in amplitude modulation, the voltage output is directly related to the resonator's movement in the magnetic field. Differential output measurement further suppressed feed-through crosstalk, providing a clearer observation of the true resonance behavior.

Jung et al.[95] developed a two-axis MEMS magnetometer utilizing an electrostatically driven eccentric resonator ($1000 \times 1000 \times 50\ \mu m^3$) and an electromagnetic inductor, which consists of 52 turns of a two-layer induction coil. Figure 5c illustrates the schematic configuration of the magnetometer, where the eccentric resonator consists of

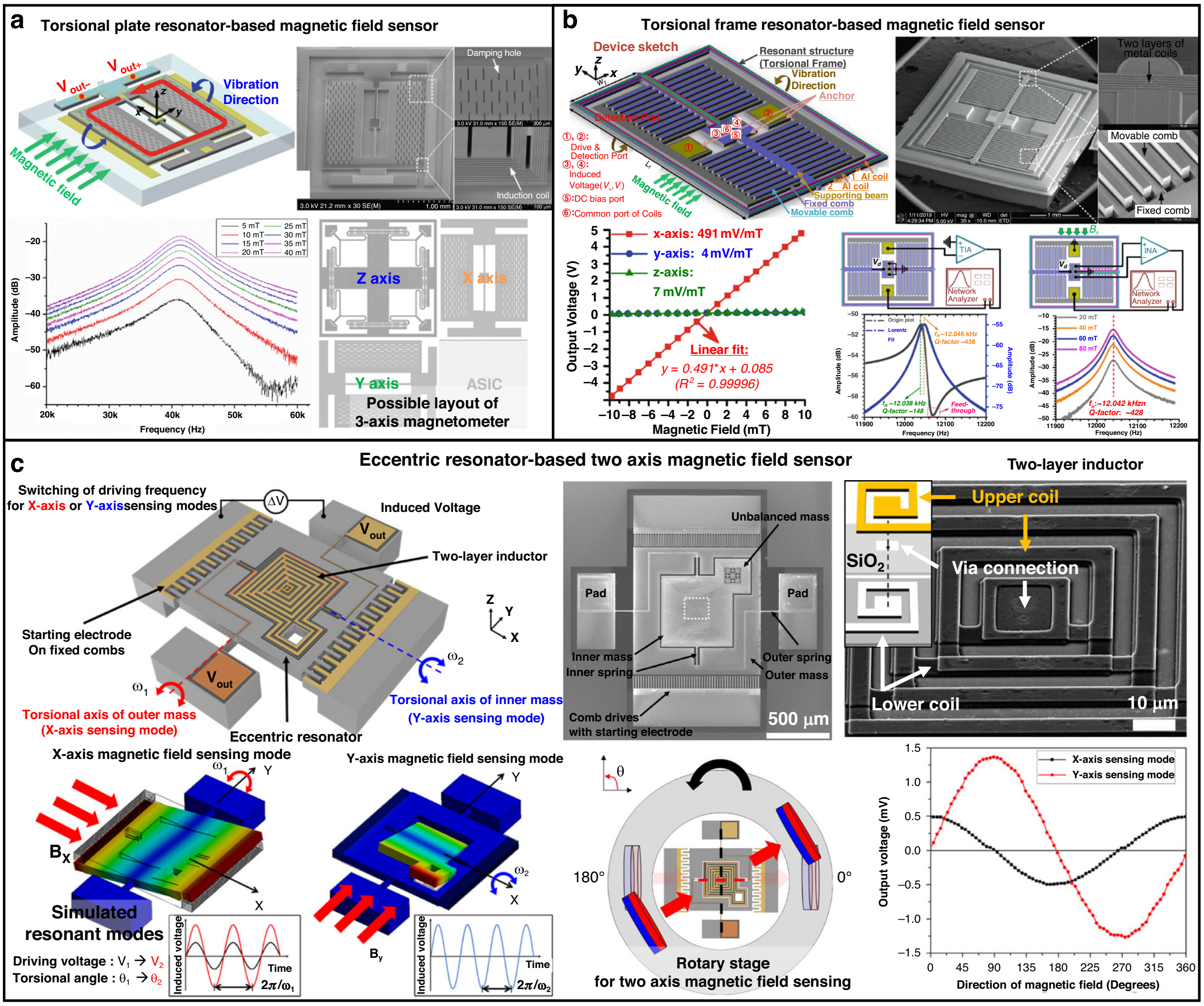

Fig. 5 In-plane MEMS magnetic field sensors driven by electrostatic force. **a** Torsional plate resonator-based sensor actuated by parallel-plate electrodes[92]. SEM images show the fabricated structure with damping holes and an integrated induction coil. **b** Torsional frame resonator-based sensor using vertically interlaced comb drives that enlarge the actuation area and reduce air damping, thereby improving sensitivity and Q-factor. Measured output responses confirm low cross-axis interference and good linearity[93]. **c** Two-axis MEMS magnetometer employing an eccentric resonator with a two-layer inductor[95]. By switching the driving frequency, torsional resonance is excited along either the X- or Y-axis and enables vector detection of in-plane magnetic fields

an outer mass and an inner mass. The inner mass is designed with an unbalanced mass, resulting in an eccentric displacement of the center of mass relative to each torsional axis. By switching the resonant frequency, the magnetometer achieves torsional resonance along either the X-axis or the Y-axis using a single-axis comb driver. Consequently, each resonant mode is selectively utilized for detecting the magnetic field along the X- or Y-axis. This monolithic MEMS magnetometer exhibits sensitivities of 21.91 and 57.92 μV/mT in the X- and Y-axis sensing modes, respectively. The output voltage increases with both the applied driving voltage and the magnetic field strength. A higher driving voltage leads to larger vibration amplitudes, which induce greater variation in magnetic flux through the induction coil. The sensor exhibits the in-plane magnetic field sensing characteristics under a driving voltage of 160 V in an atmospheric air environment. By analyzing the measured output voltage, the MEMS magnetometer determines the in-plane magnetic field vector, including both its magnitude and direction.

Table 1 summarizes the main characteristics of resonant MEMS magnetic field sensors based on electromagnetic induction published until recently. From this comparison, it is evident that out-of-plane magnetic field sensors primarily focus on single-axis sensing and have demonstrated

Table 1 Main characteristics of MEMS magnetic field sensors based on electrostatic driving and electromagnetic induction sensing

Year	Resonator type	Sensing direction	Resonator size (μm^3)	Resonant frequency	Quality factor	Packaging condition	Sensitivity without gain	Sensitivity with gain	Resolution (μT)	Nonlinearity error (%)	Actuation voltage
2013	Square extensional[89]	Out-of-plane	1000 × 1000 × 46	4.329 MHz	3700	Unsealed	–	3 μV/mT	–	–	DC 50 V / AC 1 V
2014	Double-ended tuning fork[91]	Out-of-plane	460 × 10 × 10	173.02 kHz	13840	Unsealed	–	17.7 μV/mT	–	–	DC 5 V / RF power -15 dBm
2016	Dual square extensional[90]	Out-of-plane	1000 × 1000 × 45 × 2 (Dual)	4.319 MHz	42000	Vacuum	–	47.7 μV/mT	–	1.19	DC 40 V / AC 1 V
2019	Contractive-extensional[88]	Out-of-plane	4000 × 4000 × 51	37.63 kHz	517	Unsealed	–	1306 mV/mT	2.57	0.08	DC 25 V / AC 1.5 V
2019	Torsional plate[92]	In-plane	2000 × 2000 × 50	42.404 kHz	5.3	Unsealed	–	100 mV/mT	25	0.3	DC 25 V / AC 1.5 V
2020	Torsional frame[93]	In-plane	3000 × 2500 × 50	12.042 kHz	430	Unsealed	1.9 μV/mT	491 mV/mT	6	0.4	DC 25 V / AC 1.5 V
2025	Eccentric resonator[95]	In-plane (X/Y)	1000 × 1000 × 50	X: 5.01 kHz Y: 13.53 kHz	46.8 1381	Unsealed Unsealed	X: 21.91 μV/mT Y: 57.92 μV/mT	– –	340 100	0.97 0.71	AC 160 V AC 160 V

– No description

significant improvements in sensitivity. However, for broader industrial and technological applications, three-axis magnetic field sensing with an extended sensing range is essential. Future research directions can be categorized into three primary areas: enhancing sensitivity, improving resolution, and achieving multi-directional sensing. For in-plane sensing, sensitivity and resolution can be further optimized through analytical modeling of torsional magnetic field sensors, refinement of design parameters, and the implementation of mechanical amplification via multiple mass-spring structures. Multi-directional sensing can be realized either by systematically integrating multiple single-axis magnetic field sensors or by designing sensors with distinct resonance modes that correspond to different sensing directions.

In practice, the required resolution and corresponding sensing range vary widely depending on the target application. For example, geomagnetic navigation and vehicle detection typically demand resolutions in the microtesla range, while biomedical and brain–heart magnetic monitoring require sub-nanotesla or even femtotesla sensitivity. However, the wide gap in reported resolutions among recent MEMS-based magnetic and electric field sensors mainly reflects the varying maturity levels of the underlying device technologies rather than differences in application requirements. In other words, achieving sufficiently high sensitivity and resolution at the sensor level remains one of the key challenges to enabling MEMS devices to be effectively tailored for diverse field-sensing applications.

Addressing these challenges requires improvements at the sensor-design level, particularly for electromagnetic induction-based resonant MEMS magnetic field sensors. In such devices, the induced voltage generated by the dynamic motion of the conductive structure under an external magnetic field is inherently limited by the magnetic flux coupling efficiency, structural vibration amplitude, and coil geometry. Sensitivity can therefore be enhanced by increasing the effective coil turns, optimizing conductor layout for stronger magnetic linkage, and maximizing the mechanical Q-factor through symmetric design and vacuum encapsulation. Meanwhile, thermomechanical and electronic noise can be reduced by employing optimized transduction schemes, differential readout configurations, and low-noise amplification circuits. Additionally, the resonant frequency, device size, and dynamic response speed introduce inherent trade-offs between sensitivity and bandwidth, which must be carefully balanced according to the intended application. Continuous advances in electromagnetic coupling efficiency, low-noise design, and circuit integration are essential to bridge the current resolution gap and expand the applicability of resonant MEMS magnetic field sensors across broader field-sensing domains.

Potential applications

An electrostatically actuated MEMS resonator for magnetic field sensing with electromagnetic induction has the advantages of a small device size and complementary metal–oxide–semiconductor compatibility. The effects of replacing the Lorentz force-based MEMS magnetic field sensor include low power consumption and excellent linearity. The sensing resolution of the MEMS magnetic field sensor of this type is several microtesla, and the sensing range can be expanded by using vacuum packaging[94]. Applications of this range of magnetic field sensors include rotation and position sensing, navigation, detection and guidance of vehicles, and portable electronics[59,60].

In contrast, wearable and implantable magnetic sensors for biomedical monitoring require sub-nanotesla or even femtotesla sensitivity to detect biomagnetic signals such as cardiograms or encephalograms, which currently remain beyond the practical reach of resonant MEMS sensors. Therefore, at the present stage of technological maturity, MEMS-based magnetic sensors are more suitable for external field monitoring (e.g., motion tracking, navigation) rather than direct in vivo biomagnetic detection. Nevertheless, with continuous progress in flux-coupling efficiency, mechanical Q-factor enhancement, and low-noise readout integration, resonant MEMS magnetic sensors are expected to evolve toward sensing platforms capable of capturing biomagnetic signals, thus bridging the gap between external field monitoring and biomedical magnetic sensing. Such development would also open opportunities for cross-domain integration with MEMS electric field sensors, enabling compact, low-power, and multifunctional devices for advanced biomedical and environmental monitoring. From an application perspective, resonant MEMS magnetic sensors also require careful consideration of packaging and mechanical robustness. Mechanical shocks or vibrations can perturb the resonance frequency or degrade the Q-factor, leading to performance drift[96]. Since these devices are fabricated on rigid substrates and lack structural flexibility, ensuring mechanical isolation and robust packaging is essential for stable operation in wearable or mobile systems.

Navigation and positioning

In the navigation field, MEMS-based inertial measurement units (IMUs) with nine degrees of freedom (DOFs) are used as a personal inertial navigation system (PINS) in which a 3-axis accelerometer, 3-axis gyroscope, and 3-axis magnetic field sensor are integrated into one chip. Location information is obtained by using the 9-DOF IMUs in restricted environments, such as inside buildings and in mountain valleys, where a global navigation satellite system is not available. However, IMUs are generally problematic in that a sudden position error occurs because of

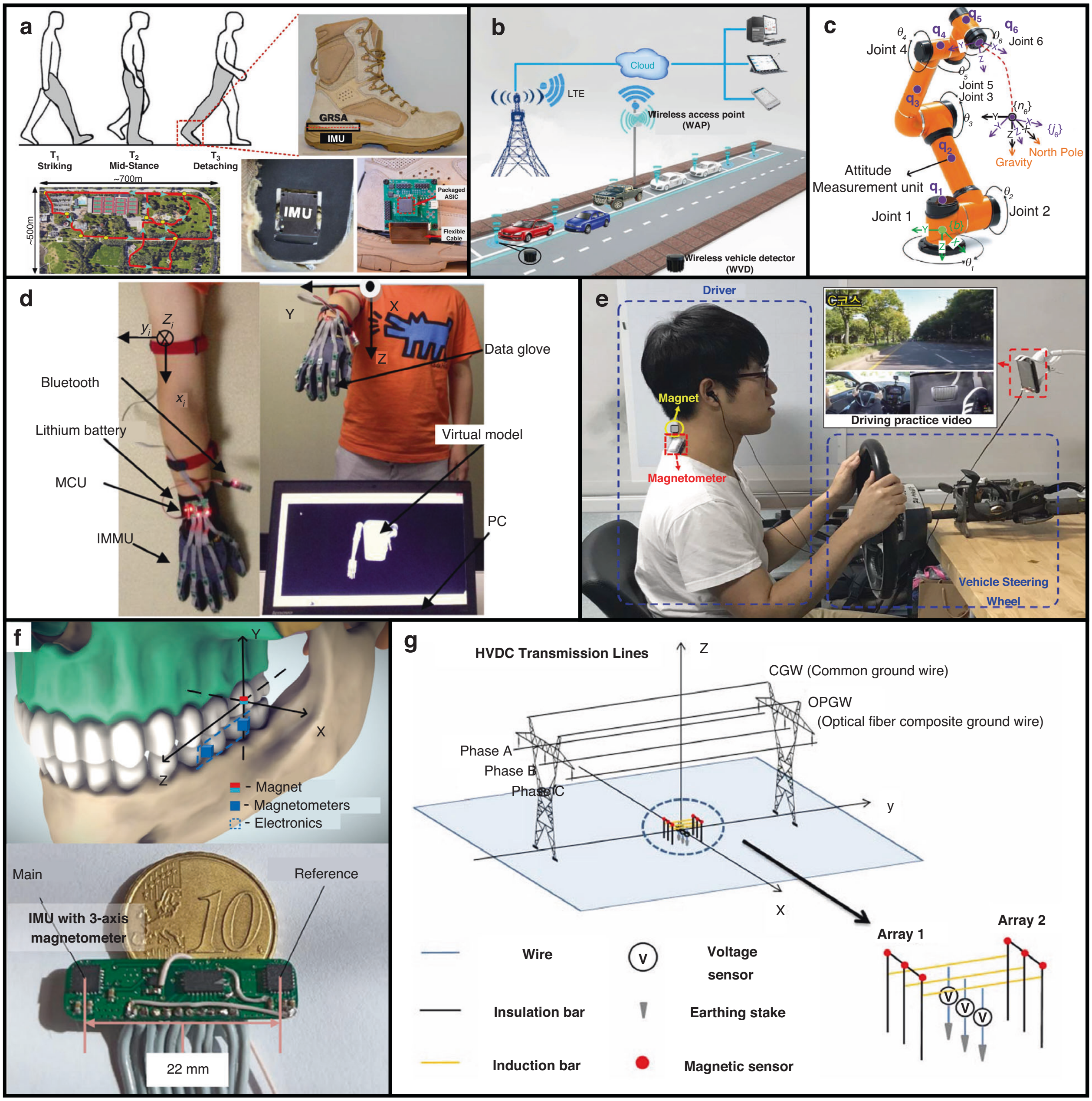

Fig. 6 Potential applications of MEMS magnetic field sensors. a PINS (personal inertial navigation system) using shoes with integrated MEMS-based 9-DOF (degree-of-freedom) IMUs (inertial measurement units) and GRSA (ground reaction sensor array)[97]. **b** Smart parking management system (SPMS) architecture provides roadside parking space information using a 3-axis magnetic field sensor[99]. **c** Robotic arm with six attitude-measurement MEMS sensors[101]. **d** Real-time gesture capture by configuring a data glove system[102]. **e** A portable sensor system that uses magnets and magnetic field sensors to monitor the driver's unbalanced head posture in driving situations[103]. **f** Concept and prototype of a wearable intra-oral magnetic sensing system for continuous jaw-motion tracking using small permanent magnets and IMUs with three-axis magnetometers. **g** Three-dimensional schematic showing the spatial arrangement of the high-voltage direct-current (HVDC) transmission lines and magnetic field sensors[104]

low accuracy, offset, and drift. Technology to compensate for this error is shown in Fig. 6a. This technology enables accurate location information to be obtained by using a ground reaction sensor array (GRSA) attached to the shoe[97], zero velocity update (ZUPT), and information that was previously mapped[98].

Vehicle detection and smart parking

In the field of vehicle detection, wireless vehicle detection was used for smart parking management systems (SPMS)[99]. Measurement of changes in the strength of the magnetic field according to the distance from a ferromagnetic object by using the magnetic field sensor made it possible to classify the arrival time, occupation time, and departure time of the vehicle[100]. Figure 6b shows that the SPMS architecture on the roadside identifies the presence of a vehicle and uses a magnetic field sensor to provide parking space information via a cloud server.

Motion tracking and posture monitoring

Figure 6c shows the robotic arm and the six attitude-measurement units (AMUs) mounted on each link. In the field of position sensing, the multi-joint angle of the revolute serial manipulator can be estimated using a low-cost MEMS magnetic, angular rate, and gravity sensor[101]. As shown in Fig. 6d, motion is captured using a data glove attached to 18 inertial and magnetic measurement units (IMMUs) worn on the hand. The motion is demonstrated immediately via a virtual model on a PC[102]. The micro-control unit attached to the data glove samples, collects, and calculates the raw data measured by the IMMUs and transmits the data to an external device via Bluetooth. The PC determines the gestures in real time based on the transmitted results and can remotely control the target to pick up, move, lift, and drop bottles using the hand of the robotic arm. Figure 6e shows an experimental system that monitors the driver's posture in a driving practice situation. A magnetic field sensor attached to the driver's neck and a small magnet detects when the posture of the head becomes unbalanced to prevent potential car accidents[103]. The magnetic field sensor measures the magnetic field along each axis according to the driver's posture in various driving situations, such as checking the road conditions to the left and right, checking the side mirrors on the left and right, and driving straight ahead. Considering the various available machine-learning methods, an algorithm was used to train a neural network to more accurately recognize the driver's current head posture based on the measured magnetic field data. Figure 6f illustrates a wearable intra-oral magnetic sensing system developed for continuous jaw-motion tracking in bruxism monitoring. The system integrates small permanent magnets with IMUs that include three-axis magnetometers to continuously register jaw position and motion trajectories. A dual-magnetometer configuration compensates for background magnetic fields, and trigonometric modeling enables the reconstruction of both translational and rotational motion. This approach demonstrates the feasibility of compact, low-power, wearable intra-oral devices capable of precise and continuous jaw-motion monitoring.

Voltage monitoring for high-voltage direct-current transmission lines

Figure 6g illustrates a non-contact voltage monitoring concept for high-voltage direct-current (HVDC) transmission lines based on hybrid electric and magnetic coupling. In this method, the voltage induced by the external electric field is correlated with the actual line voltage through magnetic-field-assisted calibration and optimization[104]. Such a sensing concept demonstrates the feasibility of DC voltage monitoring without direct electrical contact, providing a safe and scalable solution for large-area power networks. Although the reported implementation utilizes magnetoresistive sensors, similar voltage-monitoring functionality could be realized using electrostatically actuated MEMS magnetometers with electromagnetic-induction sensing. Replacing the discrete magnetoresistive components with an integrated MEMS platform would enable further miniaturization, lower power consumption, and seamless CMOS compatibility, making it suitable for array-based distributed monitoring in HVDC systems.

Electric field sensors

Electric field sensors are devices capable of detecting a wide range of electric fields, from those in the atmosphere and around the human body to those generated by electronic devices and high-voltage systems. With their versatility, these sensors have been utilized in diverse applications, including non-destructive diagnosis of electronic devices, biomedical fields, and motion sensing. From this perspective, MEMS electric field sensors have also been developed for a number of years. Methods for electric field detection using micromachined devices are based on various techniques, including electro-optical methods[105–108], steered electron detection[109], piezoelectric resonance[110], and measurements of capacitance changes resulting from electrostatic driving induced by an external field[111,112]. However, these methods often require additional power sources, which inevitably compromise the inherent miniaturization advantage of MEMS sensors. Moreover, the measured signals obtained through some of these methods are unstable and inaccurate with a low SNR. Moreover, these electric field sensors face structural and material limitations, making monolithic integration with other electronic systems difficult. In an effort to address the aforementioned issues, MEMS electric field sensors have been developed that offer a stable and linear response using simple fabrication processes. Incorporating these aspects, Wang et al. have previously provided an overview of resonant MEMS electric field sensors[113]. Instead, this paper classifies electrostatically driven resonant electric field sensors based on their target sensing dimensions and presents a structured overview of their capabilities.

Design and deployment of MEMS electric field sensors should consider the target application. For atmospheric monitoring, fair-weather fields are on the order of 100 V/m[114]. For diagnostics around HVDC or high-voltage alternating current (HVAC) assets, where events such as icing and corona onset occur, prioritize a wide dynamic range of 0–50 kV/m[115,116]. While advancing resolution and sensitivity remains important, broader utility also calls for on-chip multi-dimensional sensing that resolves unknown vector fields in hardware, together with structural cross-axis suppression.

Electrostatically driven MEMS electric field sensor using electrostatic induction

Electrostatically driven MEMS resonators for electric field sensing adopt the principle of "field mills." The field mill is a device used to sense electric fields at macroscale level, and it operates on the principle of electrostatic induction[117,118]. As shown in Fig. 7, the field mill consists of a grounded shield (or shutter) that is connected to a rotating motor, with sensing electrodes positioned beneath the shutter. Upon exposure to an electric field, a surface charge forms on the sensing electrodes, and the area exposed to the electric field is changed by rotating the grounded shield. The induced current is generated by changes in the surface charge. The surface charge density, total surface charge, and induced current on the sensing electrode are expressed by the following equations:

$$\text{Surface charge density}\,\rho_s = \varepsilon_0 E \tag{3}$$

$$\text{Surface charge Q} = \int \rho_s \mathrm{dA} \tag{4}$$

$$\text{Induced current}\,i = \frac{dQ}{dt} = \varepsilon_0 \frac{d(EA)}{dt} \tag{5}$$

where E is the applied external electric field, and A is the area of the surface exposed to the electric field. The rotating shield is grounded to prevent distortion of the electric field that needs to be detected, and a pair of sensing electrodes (denoted A and B in Fig. 7) are separately designed on the same plane and are exposed to the electric field in opposite directions. This design simultaneously induces positive and negative changes in the charge of electrodes A and B, respectively. At this time, currents in the opposite direction are induced in the two sensing electrodes according to Eq. (5). By converting the currents to voltages using current-to-voltage converters, the field mill achieves higher sensitivity in measuring the electrical potential difference through differential sensing. This electric field detection method, utilizing electrostatic induction, offers the advantages of a highly linear response and a wide detection range.

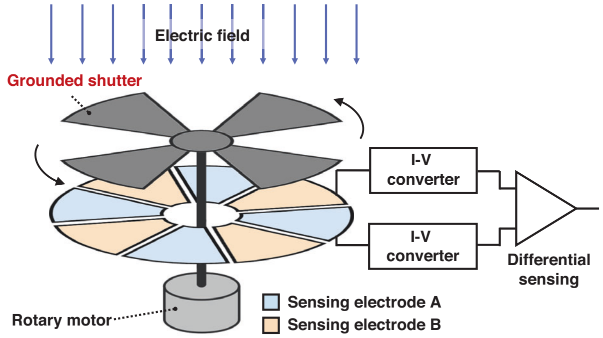

Fig. 7 Schematic diagram of a field mill at the macroscale. As the grounded shutter (or shield) rotates at a constant speed, the charge on the A and B electrodes change in opposite directions. The currents induced by these charges are generated in opposite directions. The field mill detects electric fields with high sensitivity by sensing the potential difference between the A and B electrode sets

Based on intuitive sensing principles and linear response, electrostatic induction using MEMS electric field sensors has been widely studied. However, unlike macroscale systems, achieving fully rotating motion in MEMS devices is challenging for field mill applications. To address this limitation, linear and torsional resonant driving have been applied to MEMS electric field sensors. Through lateral resonant driving of the grounded shield, the exposure area of the sensing electrodes to the electric field continuously changes, generating electrostatically induced current in the sensing electrodes.

Various alternative driving schemes in MEMS, such as electrothermal[119–122] and piezoelectric[123] methods, have been explored to achieve resonant actuation of the grounded shield. However, these methods present certain challenges, including high power consumption, complex fabrication processes, and structural limitations that result in non-IC compatible devices. Consequently, electrostatic driving, with its advantages of low power consumption and IC-compatibility, is the most commonly employed method for MEMS electric field sensors based on electrostatic induction.

One-dimensional MEMS electric field sensing

Horenstein et al.[124] designed and fabricated the first MEMS electric field sensors based on electrostatic resonance driving and electrostatic induction. This study focused on the design of a MEMS electric field sensor featuring a micro-aperture within the grounded shield. As shown in Fig. 8a, the grounded shield and the sensing electrode at the bottom face each other in a vertically parallel arrangement. The movable shuttle mass, acting as a grounded shield, has a micro-aperture ($5 \times 10\,\mu\mathrm{m}^2$) positioned within it and is anchored with folded spring structures. This grounded shield is driven with a resonant frequency of 7.6 kHz using electrostatic comb-drive actuators on both sides. The principle of electric field detection is illustrated in Fig. 8b. As the area of the sensing electrode exposed to the electric field changes, charge is induced via electrostatic induction. Despite a

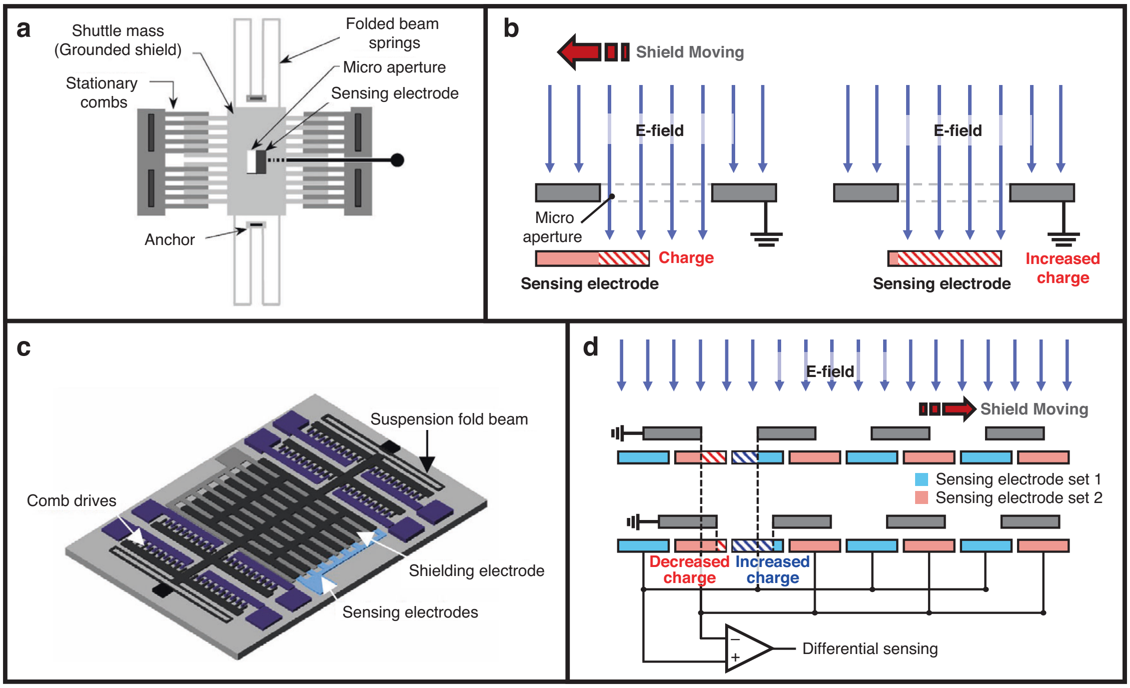

Fig. 8 MEMS electric-field sensors with a vertical parallel arrangement, where a grounded shield faces a bottom sensing electrode. **a** Schematic representation of the MEMS electric field sensor with a micro-aperture in the movable shuttle mass (grounded shield)[124]. **b** Diagram depicting electrostatic induction caused by the relative motion between the micro-aperture and the sensing electrode. The grounded shield with an aperture is electrostatically driven by the comb drive. The electric field density passing through the micro-aperture repeatedly changes, generating induced charge on the sensing electrode. The current induced by the charge variance is converted into voltage, and the sensor measures the electric field by reading the voltage. **c** Schematic of the MEMS electric field sensor based on electrostatic driving and electrostatic induction[126]. Grounded shield with slits and sensing electrodes facing each other in the vertical direction. **d** At sensing electrode set 1, the charge increases, and positive output current is induced as the area exposed to the electric field is expanded. The opposite occurs at sensing electrode set 2. The sensitivity of the sensor is doubled by obtaining the differential outputs of sensing electrodes set 1 and 2

high driving voltage of 60 V, the device exhibits low sensitivity of 35 μV/(kV/m) due to the small change in the exposed area.

Peng et al.[125,126] proposed the sensor design illustrated in Fig. 8c to enhance sensitivity by increasing the area exposed to the electric field and introducing differential sensing[127]. In this design, the grounded shield and sensing electrodes are positioned parallel to each other. The grounded shield contains multiple slits spaced apart, and comb drives resonantly actuate the shield. These slits in the shield maximize the change in the area exposed to the electric field. As shown in Fig. 8d, two large area sensing interdigital electrodes (IDEs) are placed on the bottom layer, referred to as sensing electrodes 1 and 2, and a shield with slits is actuated on the left and right in linear resonant mode by comb drives. The charge on sensing electrode 1 increases as the exposed area increases, generating a positive current. Conversely, the charge on sensing electrode 2 decreases at the same time. This arrangement enables an increase in both the SNR and sensitivity by applying differential sensing of these opposite electrical potentials.

This design, in which the sensing electrodes and the grounded shield are vertically aligned, facing each other, requires complex fabrication processes. In several studies, the sensing electrodes and the shield were integrated into the same layer in a lateral arrangement to simplify the fabrication of MEMS electric field sensors. To reduce the number of fabrication steps, Lee et al.[128], Zhu et al.[129], and Peng et al.[130] developed MEMS electric field sensors using bulk micromachining techniques with silicon-on-insulator (SOI) wafers. Figure 9a–c, respectively, presents the structural arrangement of the laterally aligned sensing electrodes and shield in an isometric view, a side view, and top-view SEM images. The sensing electrodes, grounded shield, and comb drive are incorporated into the device layer of an SOI wafer. The two sensing electrodes were arranged in opposite directions. The electric field distribution formed around the sensing electrodes changed according to the movement of the grounded shield, thereby generating charge variation. As shown in Fig. 9d, the sensing electrodes generate opposite currents based on the direction of the charge. The sensor detects the output voltage differentially by reading the voltage-converted

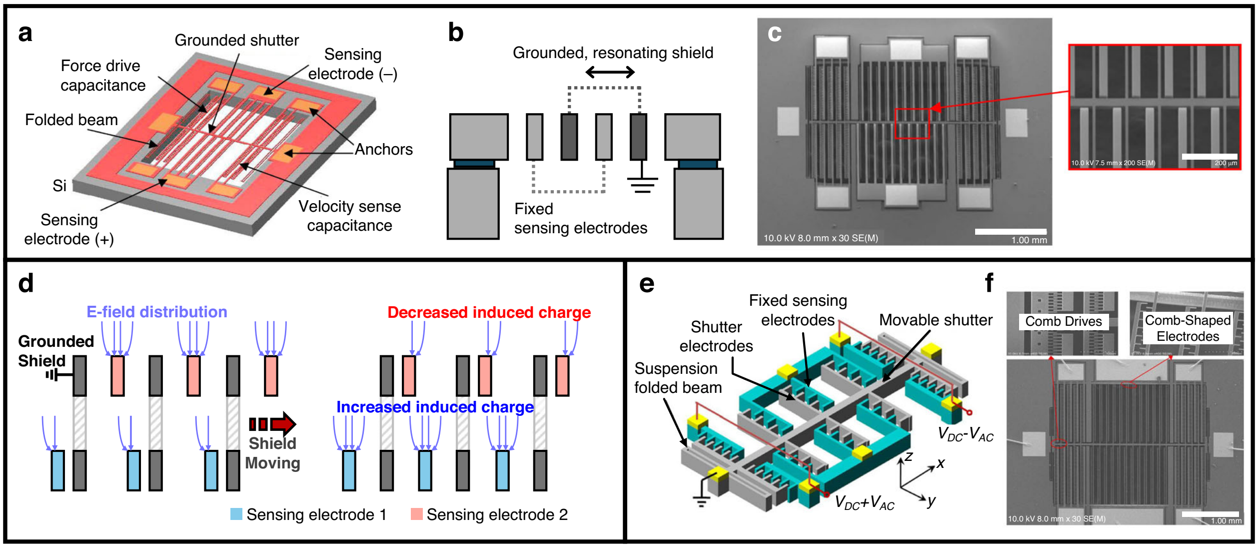

Fig. 9 MEMS electric-field sensors with laterally integrated shield and sensing electrodes. a Schematic representation of an electric field sensor structure in which the shield and sensing electrodes are arranged laterally on the same device layer[130]. **b** Cross-sectional view of an electric field sensor fabricated by a bulk-micromachined SOI wafer. **c** SEM images of the sensor. **d** Increasing the electric field density on the sensing electrode induces a positive current and vice versa. **e** Schematic of a MEMS electric field sensor using electrostatic induction[135]. The sensitivity of the sensor increases by extending the amount of charge variation with the addition of coplanar combs. **f** SEM images of the fabricated MEMS electric field sensor

signal between the two sensing electrodes. Peng et al.[130] implemented a self-oscillating closed-loop control scheme with AGC to automatically track the resonance frequency and secure high detection resolution and SNR, achieving a Q-factor of 31034 and resolution of 50 V/m. To further probe this sensing principle, Fang et al.[131] conducted a numerical analysis of the electric field distribution on the surface of the sensing electrodes when the grounded shield and sensing electrodes were placed laterally. The same structure was used to measure the synthetic electric field from atmospheric ion flow and a high-voltage system[132,133] as well as to demodulate AC/DC hybrid fields in a power system[134].

Using the same fabrication process and similar lateral structure, Yang et al.[135] improved sensitivity by increasing the capacitance between the grounded shield and sensing electrodes. In this study, coplanar comb electrodes were implemented by incorporating an offshoot structure. Figure 9e presents a schematic of the MEMS electric field sensor with coplanar comb electrodes, and Fig. 9f shows an SEM image of the device. This coplanar comb design enhances electrostatic induction, resulting in greater charge formation compared to that of a purely lateral comb. Consequently, a stronger induced current, higher sensitivity, and a resolution of 40 V/m were achieved. They also demonstrated through computational simulations that the coplanar comb structure increases charge formation.

The electric field sensors mentioned above show that integrating the sensing and shield electrodes on the same layer[128–135] has the advantage of simplifying the fabrication process. However, these sensors suffer from their relatively low sensitivity. To address this issue, Wang et al.[136] tried to increase the sensitivity of the MEMS electric field sensor by employing out-of-plane torsional resonance for the grounded shield. Figure 10 illustrates the structure and sensing principle of this sensor. Unlike previously developed MEMS electric field sensors driven by lateral comb drives, this design uses torsional resonant actuation through electrostatic forces between a pair of large-area electrodes (1900 × 500 μm^2) on the bottom and the shield, as shown in Fig. 10a, b. Figure 10c illustrates the sensing mechanism of the sensor. Vertical displacement between the shield and sensing electrodes, caused by resonant electrostatic driving, generates both charge and induced current. Makihata et al.[137] demonstrated that the efficiency of the induced current increases when the shield undergoes vertical angular movement rather than lateral movement using a multi-resonance mode MEMS device. This improved induced current efficiency enhances the sensitivity of this MEMS electric field sensor achieving 4.82 mV/(kV/m) as shown in the plot of Fig. 10d[136]. For applying the sensitivity enhancement mechanism based on torsional driving of grounded shield while simplifying the sensor structure and fabrication process, Jung et al.[138] introduced a MEMS electric field sensor in which the comb-drive actuator with starting electrode, shield, and sensing electrodes were laterally arranged. Figure 10e, f shows schematic and an SEM

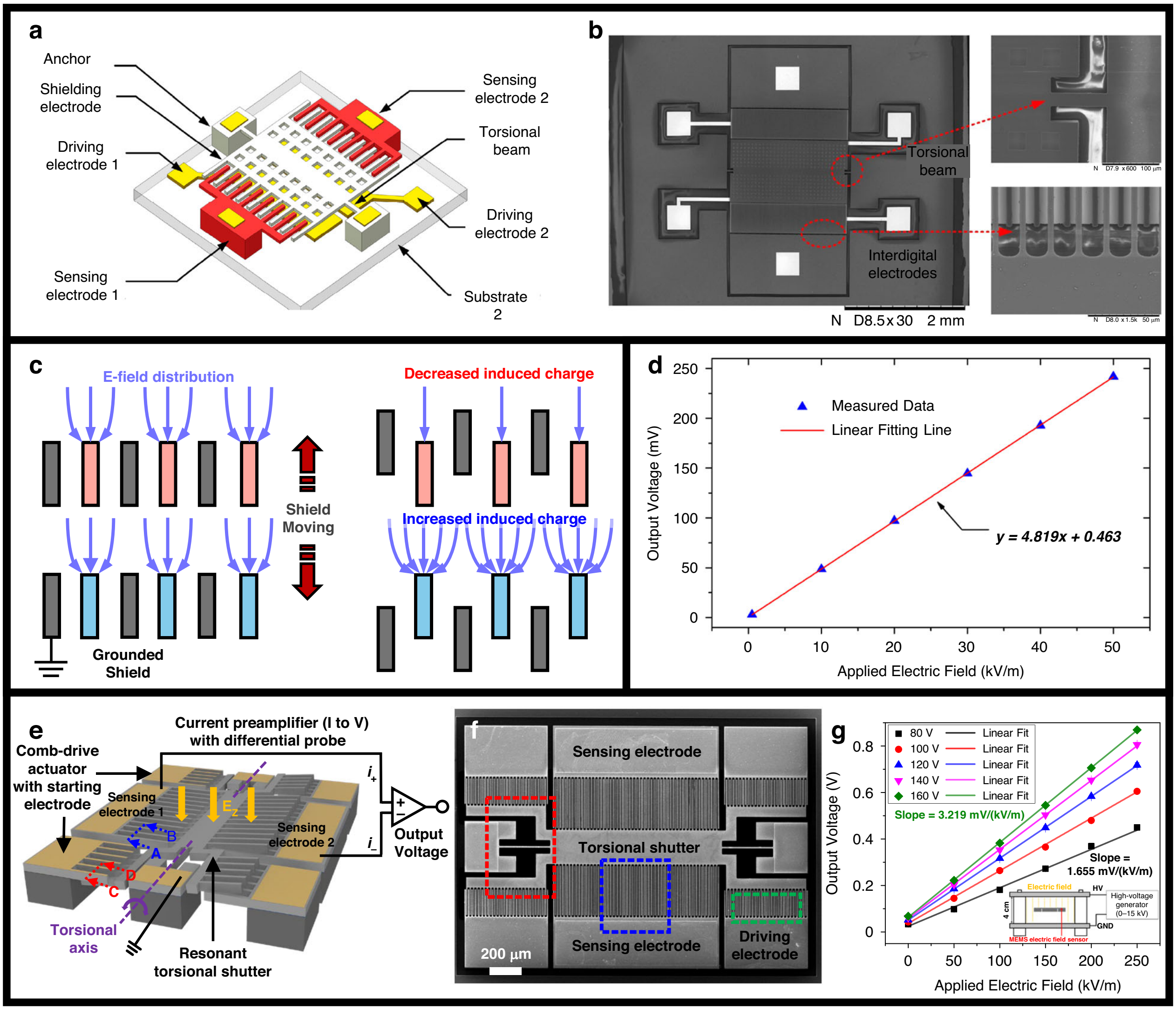

Fig. 10 MEMS electric-field sensors using out-of-plane torsional resonance of grounded shield. a Structure of the electric field sensor with out-of-plane torsional driving via an electrostatic force between the driving electrode at the bottom and the grounded shield[136]. **b** SEM images of the MEMS electric field sensor with a torsion-driven shield. **c** Movement of the grounded shield results in vertical displacement between the shield and the sensing electrode. At this time, the distribution of the electric field reaching the sensing electrode changes. This generates an induced current on the basis of changes in the charge. **d** Response plot of the MEMS electric field sensor. **e** A schematic illustration of the MEMS electric field sensor with torsional comb driving[138]. **f** A SEM image of the sensor showing lateral integration of sensing and driving electrodes. **g** Sensor responses under different driving voltages

image of this MEMS electric field sensor. The sensor places the driving electrodes, sensing electrodes, and a torsional shutter on the same layer, while designing the sensing electrodes with a high aspect ratio to maximize the area exposed to the electric field during resonant driving. With this design, as depicted in Fig. 10g, the MEMS sensor achieved a response of 3.219 mV/(kV/m).

Multi-dimensional MEMS electric field sensing

In the previously described MEMS electric field sensors, the electric field was measured by applying it in a single direction. However, in many scenarios, such as in autonomous driving, the direction of the electric field measurement is unknown. Thus, a need has arisen to measure a multi-dimensional electric field. To address this challenge, MEMS sensors capable of detecting multi-directional electric fields have been developed.

Wang et al.[139] developed a two-dimensional electric field sensor on a single chip driven by a single electrostatic actuation, as shown in Fig. 11a–d. This electric field sensor features a symmetrical structure on all four sides. Each side consists of a central rotary comb drive, an

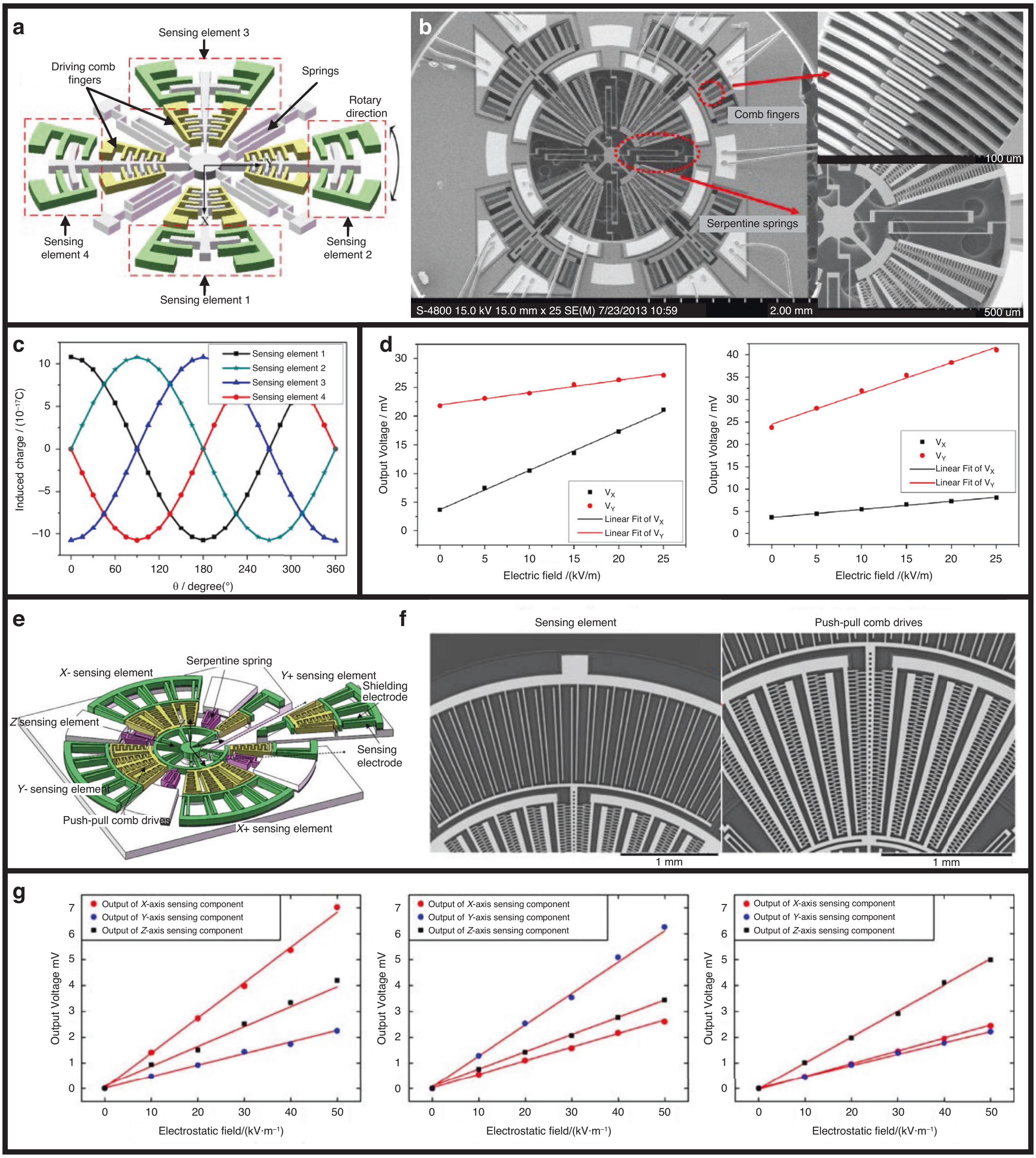

Fig. 11 Single chip MEMS sensors for multi-dimensional electric-field measurement. a Schematic illustration of a MEMS 2D electric field sensor consisting of four pairs of driving and sensing parts[139]. **b** SEM images of the fabricated electric field sensor. **c** Simulated induced charge for the four sensing elements versus the incident angle of an external electric field. **d** Results of the X-axis (left) and Y-axis (right) electric field measurement. The black squares and red dots are the responses of the X- and Y-axis sensors, respectively. Both of these results are affected by cross-interference with other axes, requiring additional calibration. **e** Structure of the MEMS 3D electric field sensor with single driving input consisting of rotary comb drives in four directions[140]. The sensor has X- and Y-sensing components on the outside and Z-axis sensing components at the center. **f** SEM images of the sensing and driving parts of the sensor. **g** Measured output voltage as a function of the electrostatic field: X-axis (left), Y-axis (middle), and Z-axis (right). As seen above, cross-interference also occurs when the electric field of all axes is detected

external sensing element, and a grounded shield-sensing electrode pair. The grounded shield is rotationally driven by the four comb drives. The sensing element pairs labeled 1–3 and 2–4 in Fig. 11a detect electric fields in the X- and Y-directions, respectively. In addition, as shown in Fig. 11c, two sensing elements in a directional pair produce signals of equal amplitude with opposite phase, enhancing sensitivity through differential sensing. The magnitude and direction of the two-dimensional electric field can be determined by the vector summation of the X-axis electric field (E_X) and Y-axis electric field (E_Y). With this mechanism, sensitivities of 0.675 mV/(kV/m) and 0.689 mV/(kV/m) were achieved on the X- and Y-axes, respectively. To perform 2D sensing with only a single actuation, electrostatic rotary comb driving is used instead of linear movement along the X- and Y-axes. In this situation, cross-interference from the electric fields along the other axis inevitably appears (the red line connecting the dots on the left and black line connecting the squares on the right in Fig. 11d).

Ling et al.[140] developed a MEMS sensor for three-dimensional (3D) electric field sensing driven by single electrostatic resonance. A Z-axis sensing function was added by placing a pair of grounded shield-sensing electrodes at the center. This sensor, depicted schematically in Fig. 11e, has four side symmetrical rotary comb drives and external sensing comb electrodes and a central component for Z-axis sensing. Figure 11f presents SEM images of the fabricated sensor's sensing and driving parts. Figure 11g shows the sensing characteristics of the electric field along each axis. This MEMS 3D electric field sensor has a relatively large footprint area ($1100 \times 1100\ \mu m^2$) and volume. Therefore, the sensor requires high-voltage electrostatic driving of DC 80 V and AC 3.5 V to drive its large mass. Its sensitivities are 0.136, 0.121, and 0.101 mV/(kV/m) for the X-, Y-, and Z-axes, respectively. However, undesirable cross-interference inevitably occurs among the axes as it is a 3D electric field sensor driven by single rotary resonance.

This interference results in signals from other axes reaching half the intensity of those from the target axis[139,140]. Within these single chip architectures, traditional mathematical decoupling calibration methods can be applied to separate axis components and compensate cross-interference[141,142]. To further exclude cross-axis interference, statistical estimators such as recursive least-squares and maximum-likelihood can be used to identify bias, scale, and misalignment parameters[143]. Beyond these statistical model-based approaches, data-driven algorithm based decoupling has also been explored: for example, genetic-algorithm (GA) optimization can identify decoupling parameters that minimize cross-axis error across the operating envelope[142], and multi-output support vector machine (SVM) regression can map measured vectors directly to the true 2D and 3D field with improved robustness[144]. Together, these algorithmic pathways offer a practical route to compact multi-axis electric field sensors while avoiding footprint growth and complex post-fabrication processes.

To address cross-axis interference inherent to on-chip electric field sensors, Ling et al.[145] designed a new electric field sensing device utilizing physical integration of three separate electric field sensors to minimize cross-interference with the other axes. In this study, one-dimensional (1D) MEMS electric field sensors were fabricated to measure the lateral electric field, as shown in Fig. 12a. The three 1D electric field sensors were then attached to a printed circuit board (PCB, $3 \times 3\ cm^2$), and they were manually combined in an orthogonal arrangement like Fig. 12b. The driving voltage was DC 20 V and AC 1 V, and three sensors were designed to operate at same resonant frequencies. All three sensors are driven by a single input with the same voltage and frequency. The 3D electric field sensor manufactured in this way detects 3D electric fields with very low cross-interference, as shown in Fig. 12c.

However, this manually combined electric field sensor is bulky and requires a laborious assembly process with low reliability. Ling et al.[146] therefore developed a MEMS electric field sensor by fabricating three 1D electric field sensors simultaneously on a wafer-scale to facilitate simple assembly. As seen in Fig. 12d, three electric field sensors are connected by micro-hinges made from a photosensitive polyimide (PSPI) film. These hinges enable precise manufacturing without assembly misalignment. The resonant frequencies of the three sensors were intentionally designed to be similar, resulting in 2270, 2245, and 2210 Hz for the X-, Y-, and Z-axes, respectively. This sensor has three 1D electric field sensors arranged in a self-assembled isosceles right triangle configuration for 3D electric field detection (Fig. 12e). However, as shown in Fig. 12f, the electric field in the Z-axis causes cross-interference during sensing in the X- and Y-axes directions.

Table 2 summarizes the electrostatic induction utilized by the electrostatically driven MEMS electric field sensors discussed above. The summary includes the driving conditions and sensing performance of these sensors. Due to the linearity of their sensing mechanism, they exhibit linear measurement characteristics with a linearity error of less than 5.5%. In addition, multi-dimensional electric field detection with MEMS sensors has been attempted over time. However, from a sensing performance perspective, the overall sensitivities of these multi-dimensional electric field sensors are low. As a result, electric field sensing circuits require voltage amplifiers. The minimum reported sensing resolution is 40 V/m, indicating that further improvement in sensitivity and

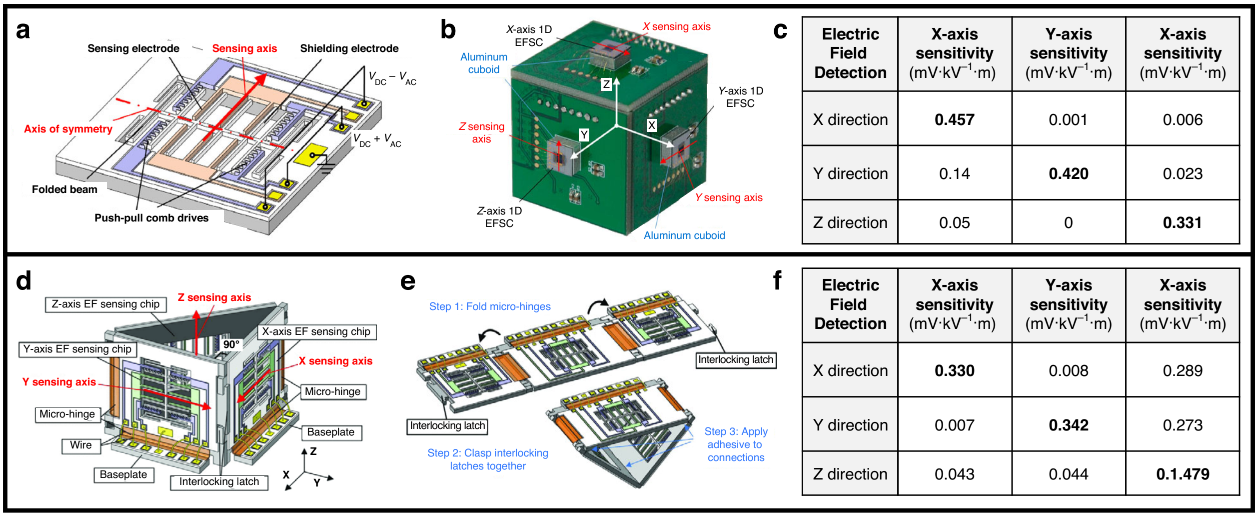

c

Electric Field Detection	X-axis sensitivity (mV·kV^{-1}·m)	Y-axis sensitivity (mV·kV^{-1}·m)	X-axis sensitivity (mV·kV^{-1}·m)
X direction	**0.457**	0.001	0.006
Y direction	0.14	**0.420**	0.023
Z direction	0.05	0	**0.331**

f

Electric Field Detection	X-axis sensitivity (mV·kV^{-1}·m)	Y-axis sensitivity (mV·kV^{-1}·m)	X-axis sensitivity (mV·kV^{-1}·m)
X direction	**0.330**	0.008	0.289
Y direction	0.007	**0.342**	0.273
Z direction	0.043	0.044	**0.1.479**

Fig. 12 Electric field sensors with physical integration of three discrete sensors to minimize cross-axis interference. a Schematic of the 1D MEMS electric field sensor for use as a 3D electric field sensor[145]. These 1D sensors are physically integrated perpendicularly. **b** Optical image of the 3D electric field sensing device with three 1D sensors combined on a PCB and placed perpendicularly to each other. **c** Electric field detection results. Cross-interference with the detection results of other axes is significantly reduced compared to the multi-dimensional electric field sensors based on single driving input. **d** Schematic of the 3D electric field sensor folded to combine three 1D electric field sensors after combination[146]. **e** Process of bonding three 1D sensors using polymer hinge bonding after on-wafer fabrication. **f** As a result of electric field detection, cross-interference on the Z-axis detection increased owing to structural limitations

resolution is necessary for reliable electric field detection and broader applications.

Electrostatically driven MEMS electric field sensor using mode localization

Mode localization-based MEMS sensors measure the frequency change in the resonant mode of weakly coupled resonators. When an input, such as mass[147] or acceleration[148], is applied, a small perturbation occurs and shifts the resonant frequency of the coupled system. Using this phenomenon, Hao et al.[149] demonstrated a mode localized MEMS electric field sensor. Figure 13a, b shows a schematic illustration and a SEM image of the mode localized MEMS electric field sensor with electrostatic resonators, respectively. Resonator 1 and resonator 3 have same dimensions, and all three resonators, including resonator 2, are weakly coupled. The frequency responses from the sense ports, shown in Fig. 13c, display two peaks corresponding to the first two vibration modes of the weakly coupled system. In the first mode, resonators 1 and 3 vibrate in the same lateral direction, while in the second mode, they move in opposite direction. When an external electric field is applied, electrostatic force displaces the movable comb in the capacitor array, inducing electrostatic negative stiffness. This stiffness perturbation produces small peak shifts and drastic change in the amplitude ratio of two modes in the frequency responses. The induced amplitude ratio has a linear relationship with the magnitude of the external electric field, and the mode localized MEMS electric sensor demonstrated a sensitivity of 0.76 /(kV/m) within the sensing range of 7 kV/m.

Potential applications

Electrostatic resonant driving and electrostatic induction using MEMS electric field sensors are CMOS-compatible because of their simple structures and fabrication process[150]. Thus, these sensors can be easily integrated into various electronic systems. Figure 14 shows typical applications of MEMS electric field sensors.

HVDC transmission lines monitoring

Because of their wide electric field sensing range, electrostatic induction type MEMS sensors are suitable for diagnose high-power systems such as HVDC transmission lines[151–153]. Figure 14a shows optical images of an electric field detection package and an HVDC system. The electric field detection package consists of a sealed MEMS electric field sensor, central processing unit (CPU), a telecommunication module and a housing metal box. The output signal obtained from the sensor is transmitted to the CPU inside the metal box for data processing. The processed data, along with locational information, is then sent to an external power-monitoring center to diagnose the HVDC system's condition.

Nondestructive circuit diagnostics

MEMS electric field sensors can also non-destructively monitor electric circuits, even small smart mobile devices[154].

Table 2 Comparison of electrostatic induction-type MEMS electric field sensors that are electrostatically driven

Year	MEMS electric field sensor characteristics	Sensing axis	Resonator size (μm^3)	Resonant frequency	Quality factor	Packaging condition	Sensitivity (mV/(kV/m))	Resolution (V/m)	Nonlinearity error (%)	Actuation voltage	Sensing range (kV/m)
2001	Vertical design with aperture[124]	1D	120 × 80 × 2	7.6 kHz	–	Unsealed	0.035	–	–	DC 60 V/AC –	500
2006	Vertical design with slit[126]	1D	400 × 560 × 2	4.13 kHz	10	Unsealed	18.3	200	1.8	DC 20 V/AC 0.3 V	10
2010	Lateral design[130]	1D	–	1.862 kHz	31034	Vacuum	0.09	50	2.1	DC 0.25 V/AC 0.02 V	50
2013	Coplanar-lateral design[135]	1D	2700 × 2200 × 25	3.042 kHz	–	Unsealed	0.2	40	1	DC 20 V/AC 1 V	50
2018	Bottom-actuated torsional[136]	1D	1900 × 2000 × 10	5.190 kHz	10.81	Unsealed	4.82	–	0.15	–	50
2025	Comb-actuated torsional[138]	1D	2000 × 800 × 50	7.43 kHz	–	Unsealed	3.219	1667	0.7	AC 160 V	250
2015	2D detection with single driving[139]	2D	3500 × 3500 × 25	799 Hz	27	Unsealed	X: 0.675, Y: 0.689	–	1.41	DC 40 V/AC 1 V	25
2017	3D detection with single driving[140]	3D	7000 × 7000 × 20	1.291 kHz	–	Unsealed	X: 0.136, Y: 0.121 Z: 0.101	–	5.5	DC 80 V/AC 3.5 V	50
2018	3D detection with 3 assembled sensors[145]	1D	2600 × 2000 × 25 for X, Y and Z	X: 2.22 kHz, Y: 2.22 kHz, Z: 2.25 kHz	–	Unsealed	X: 0.457, Y: 0.420, Z: 0.331	–	1.8	DC 20 V/AC 1 V	120
2019	3D detection with 3 assembled sensors[146]	1D	2600 × 2000 × 25 for X, Y and Z	X: 2.27 kHz, Y: 2.25 kHz, Z: 2.21 kHz	–	Unsealed	X: 0.330, Y: 0.342, Z: 1.479	–	4.3	DC 20 V/AC 1 V	120
2022	Mode localization[149]	1D	$(2.57 \times 10^6) \times 30$	24 kHz	25000	Vacuum	0.76/kV/m	22.9	0.16	DC 5 V/AC 5 mV	7

– No description

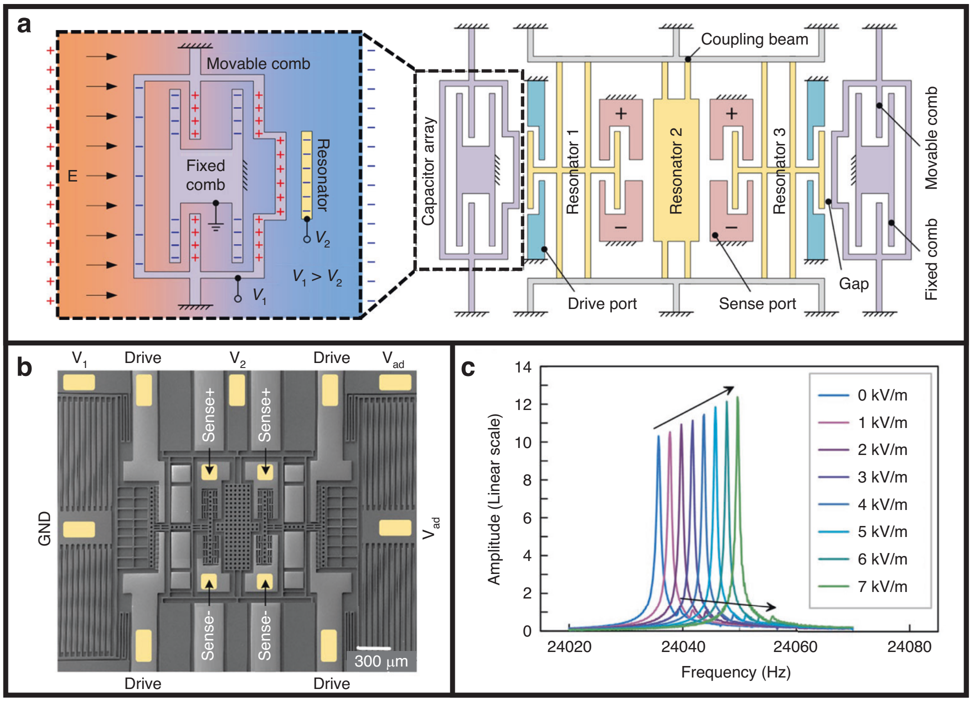

Fig. 13 Mode localized MEMS electric field sensor. a Schematic of the mode localized electric field sensor when external electric field applied[149]. **b** A SEM image of the fabricated electric field sensor. **c** Frequency responses of the electrostatic resonator 1 when an external electric field of various sizes enters up to 7 kV/m

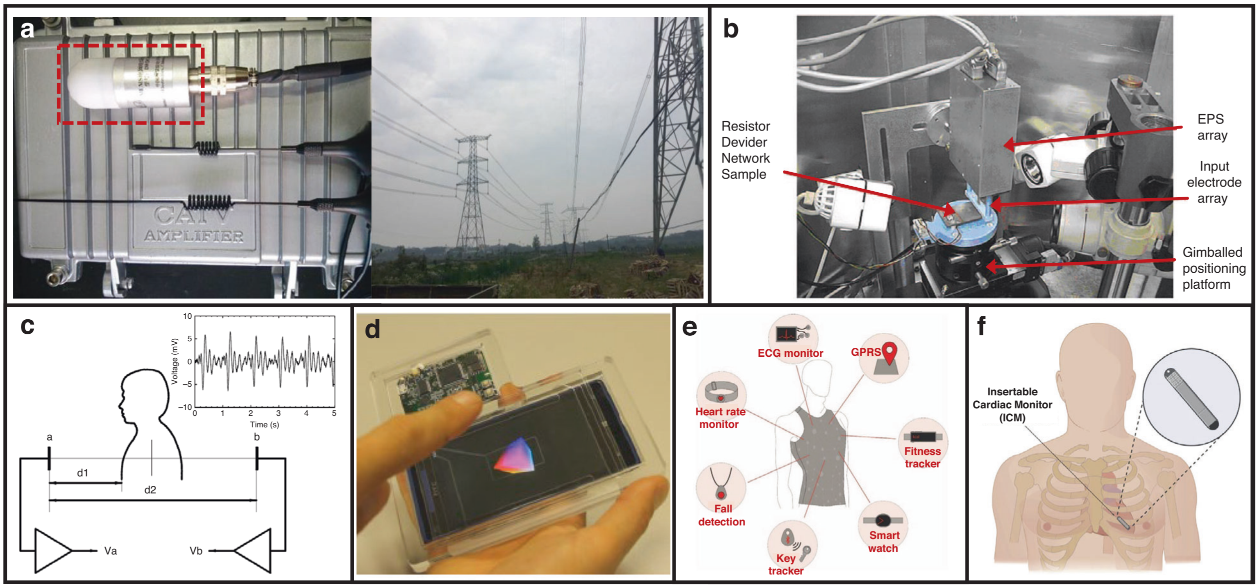

Fig. 14 Potential applications of MEMS electric field sensors. a Packaged setup containing MEMS electric field sensor for diagnosis of HVDC system[153]. The white package in the red box includes a CPU integrated with an electric field sensor. **b** Non-destructive diagnosis of a resistor divider network with an electrical potential sensor array[154]. **c** ECG diagnosis using an electrical potential probe. Electric field detection with MEMS can be applied to detect bioelectric signals to compactly diagnose human health[156]. **d** Hand tracking of mobile electronic devices using the built-in electric field sensor array[158]. **e** Schematic of wearable electro clothing system[161]. **f** Illustration of an implantable ECG loop recorder[164]

Figure 14b shows an example of the non-destructive diagnosis of a resistor divider using an electric potential sensor array. The sensor array was used to perform electric field map imaging of the circuit. In addition to electric systems, they are used for the diagnosis of equipment that excites magnetic fields[155].

Bioelectric interfaces and health monitoring

Furthermore, bioelectric measurement applications, such as an electrocardiogram (ECG), electroencephalography (EEG), and electromyography (EMG), are possible[156,157]. Figure 14c shows an example of an ECG measurement, where the sensor detects changes in the electrical properties corresponding to heart rate, enabling non-contact monitoring of blood flow. These sensors can detect electric fields around all electrically charged objects, including living organisms. The sensors can perform hand tracking, as shown in Fig. 14d[158,159].

Wearable and implantable medical devices

Leveraging miniaturization, low power, high-reliability signal sensing, and CMOS compatibility, electric field sensors can be applied to wearable and implantable electric potential-tracking applications. Figure 14e illustrates the concept of a wearable clothing system that uses electric field sensors to measure diverse bioelectric signals across the body. They can support health monitoring such as ECG[160], as well as activity monitoring and proximate-object detection[161]. In addition, miniaturized MEMS electric field sensors can be integrated with catheters for accurate guidance of medical tools[162] or implanted for therapeutic applications, including ECG loop recorders[163,164], as shown in Fig. 14f. However, implantable applications face challenges such as field screening in tissue[165], motion artifacts[166], long-term drift and packaging limits[167]. Additional shielding strategies[168] and bio-stable thin-film encapsulation[169] can ensure reliability and thereby enhance operational stability.

Technical challenges and application prospects of integrated MEMS sensors for simultaneous magnetic and electric field detection

So far, we have reviewed the working mechanisms, sensitivity-enhancement strategies, and classifications by drive axis and sensing dimension for electrostatically resonant MEMS magnetic and electric field sensors. In these devices, electrostatic actuation drives the resonator, and the external field is encoded via electromagnetic induction for magnetic sensing and electrostatic induction for electric sensing. Because the two sensors share CMOS-compatible processes and similar readout structures, co-integration is straightforward, allowing either a single resonant structure or tightly co-located structures to serve as a compact multi-modal sensing platform. Bringing both channels onto one chip enables sensor fusion that combines redundancy and complementarity, improves robustness to drift and interference, and preserves low power and a minimal footprint.

While the two MEMS sensors share CMOS-compatible processes, co-integration introduces coupled effects that must be managed. For example, feedthrough from parasitic capacitance[170,171] and eddy currents[172,173] can cause crosstalk and intermodulation, while bias-induced softening, dielectric charging, and temperature gradients introduce slow drift[36]. Another practical issue is the dual front ends: to stay low noise and well isolated, they benefit from strong common-mode rejection[174] and calibration that identifies the coupling matrix across temperature and bias[175]. In addition, in strong electric or magnetic environments, the dominant field can saturate electronics, reduce effective dynamic range, so shielding and range protection are required[176,177]. Taken together, these measures make single-chip simultaneous electric and magnetic field sensing more robust and open the door to applications in autonomous mobility, power-infrastructure diagnostics, and wearable bio-monitoring systems.

MEMS sensors integration for advanced autonomous mobility

With an integrated platform that measures both fields at once, the observation space naturally widens where cameras, lidars, and radars tend to struggle. Electric field sensors capture short-range context to a few tens of centimeters at very low power[178], while the magnetic-field channel provides directional and positional cues through interactions with geomagnetic maps or infrastructure markers. Autonomous driving makes the flow concrete. In tunnels, urban canyons, or heavy snowfall where global positioning system (GPS) is weak, magnetic cues fuse with wheel odometry and IMU to bound position drift[179–181]. At very close range, safety and interaction are handled by the electric field channel. Door and edge proximity, connector approach, and targets that are difficult for vision, such as transparent or very dark objects, can be sensed reliably as changes in the electric field[182]. Using proximity detection and electromagnetic field sensing, the same approach can be applied to wireless electric vehicle (EV) battery charging platforms, as illustrated in Fig. 15a. During wireless power transfer parking, magnetic patterns estimate coil alignment and coupling, while electric field measurements monitor stray exposure and foreign objects, so alignment feedback and exposure compliance can be achieved together[183,184]. The compact, lightweight, and ultralow-power MEMS form factor also suits small unmanned aerial vehicles (UAVs) where payload and power budgets are tight. In that context, joint electric and magnetic sensing can support GPS-degraded navigation assistance, close-range obstacle awareness, and safe alignment with wireless charging pads on docking stations[185,186]. The result is fewer perception gaps in bad weather, glare, or scenes with reflective or transparent materials.

Energy infrastructure monitoring

Power and energy infrastructure also benefit from integrated MEMS sensing. In real electromagnetic settings both magnetic and electric fields coexist, so measuring only one gives an incomplete picture and motivates sensing of both with spatial correlation for compact and reliable characterization at high spatial and temporal resolution. Separate sensors often struggle with alignment and stability, whereas electrostatically actuated MEMS offer a common platform where induced charge supports electric sensing and induced current supports magnetic sensing, letting one structure collect signals coherently while keeping footprint and complexity low. For power assets the electric channel surveys ground fields while the magnetic channel tracks changes tied to operating states and fault signatures. Joint acquisition enables non-destructive diagnostics, localization, and safety alerts within one package[187]. At the application level, UAV inspections show both promise and the limits of single modality sensing. Electric field systems map potentials and assess insulation with capacitive plates[188], while magnetic systems use line flux to estimate conductor distance and orientation for navigation[189,190], as illustrated in Fig. 15b, c, respectively. Each approach captures only part of the scene, so recent studies combine both to describe coupled phenomena[191]. One approach computes the Poynting vector from measured fields and uses its direction and magnitude for UAV guidance[192]. Simultaneous and co-located measurement delivers richer and more correlated information than either modality alone, and electrostatically resonant MEMS offer a practical path to that integration.

Biomedical multimodal diagnostics

In biomedicine, simultaneous recording of an electrical modality (EEG, ECG, and EMG) with its magnetic counterpart is used to improve source localization, denoise common-mode artifacts, and add diagnostic markers that are invisible to a single channel. For the brain, recent wearable magnetoencephalography (MEG) and EEG systems demonstrate that co-recording does not degrade signal quality, opening avenues for bedside monitoring[193,194]. For the heart, as shown in Fig. 15d, simultaneous ECG and magnetocardiography (MCG) sharpened arrhythmia risk assessment[195,196]. For muscle, EMG and magnetomyography (MMG) pairs capture complementary spatial selectivity and depth information[197,198] (Fig. 15e). These precedents suggest that a single-chip, co-registered MEMS magnetic and electric sensors could miniaturize such dual-modality diagnostics, toward ambulatory neuro-, cardio-, and neuro-muscular monitoring, while reducing cost and power consumption.

Within this emerging context, electrostatically actuated MEMS resonators represent a promising technological bridge. Their ability to sense both induced charge and induced current within a unified mechanical platform offers a scalable path toward realizing this conceptual convergence at the microscale. Integrating these principles could enable truly co-located and phase correlated field measurements while laying the groundwork for next generation high precision and autonomous inspection systems capable of comprehensive electromagnetic diagnostics.

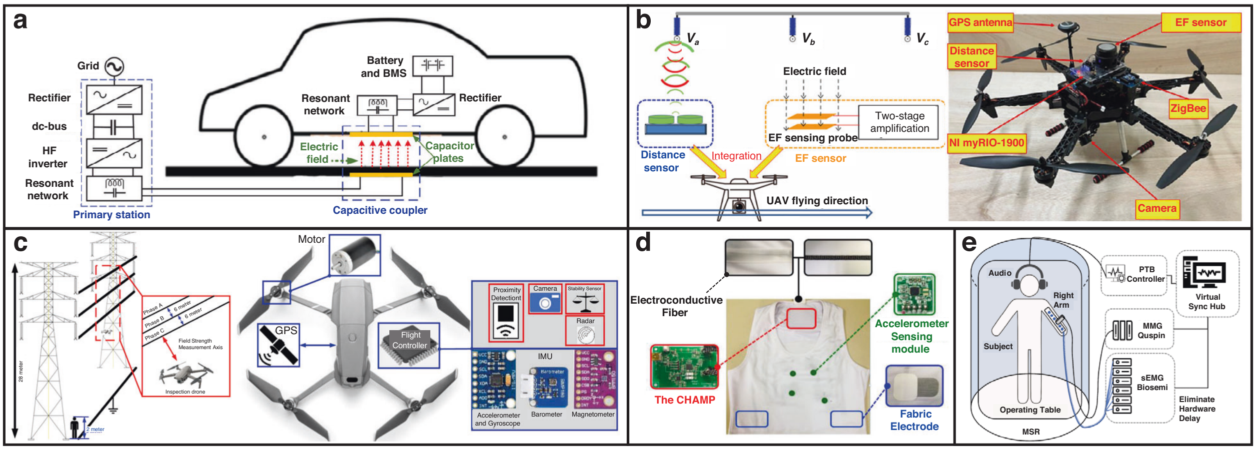

Fig. 15 Applications of MEMS magnetic and electric field sensor integration. a Schematic diagram of a capacitive wireless charging system for EV alignment[183]. **b** Schematic diagram and photograph of an unmanned aerial vehicle (UAV)-based electric field measurement system for inspecting transmission line[188]. **c** UAV-based magnetic field measurement technology near double circuit transmission line structures[190]. **d** Photographs of smart clothing for simultaneous ECG and MCG acquisition[196]. **e** Schematic diagram of a multimodal system that synchronously acquires surface EMG and MMG for muscle activity analysis[198]

Conclusions

In this paper, we reviewed MEMS magnetic and electric field sensors with electrostatic resonators. Electrostatic actuators, known for their low power consumption, ease of fabrication, and structural versatility, can induce various motion types in different vibrational modes, such as linear and torsional movements. As described above, magnetic fields are measured by the induced electromotive force generated in an induction coil when the effective area of the magnetic field changes with lateral or torsional electrostatic driving. Electric fields, on the other hand, can be measured through electrostatic induction by using electrostatically resonant driving of a grounded shield to change the electric field distribution reaching the sensing electrodes. Additionally, a mode localized MEMS electric field sensor with weakly coupled electrostatic driving resonators was also reported.

Recently, many MEMS magnetic and electric field sensors have been developed to detect accurate vector information of target fields with high sensitivity, wide sensing ranges, and multi-axis field detection. However, cross-interference is a recurring issue in multi-axis detection, requiring additional external calibration. Despite these challenges, the simple structures of electrostatically driven MEMS magnetic and electric field sensors, combined with their voltage output, make them CMOS-compatible and easy to read target signals.

Further performance enhancement can be achieved through advances in closed-loop resonance control, nonlinear dynamic compensation, and signal conditioning. These control strategies are effective in stabilizing resonance amplitude, mitigating electrostatic stiffness nonlinearities, and suppressing residual electronic noise, thereby improving the SNR and enhancing overall operational robustness.

At the device level, performance improvements will also increasingly depend on fabrication precision. Machining imperfections such as thickness nonuniformity or slight mass imbalance can induce frequency split between degenerate vibration modes, leading to standing-wave drift and output errors[199]. Therefore, ensuring axisymmetric mass and stiffness distribution through intentional structural design and precision-controlled fabrication is crucial for achieving frequency stability and long-term reliability. In MEMS fabrication, this can be realized through wafer-level techniques that improve dimensional accuracy and surface quality while preserving batch compatibility.

In particular, advanced etching and planarization processes are key to enhancing the structural uniformity of resonant MEMS sensors. For instance, deep reactive ion etching (DRIE), which enables deep and highly anisotropic silicon etching, must be precisely controlled to minimize sidewall scalloping and etch-depth variations that can alter effective stiffness and shift the resonance frequency[200,201]. Complementary to this, chemical–mechanical planarization (CMP) reduces surface roughness and ensures uniform mass distribution, providing a smooth surface for thin-film deposition, enabling precise resonance control, and improving frequency stability[202,203]. These wafer-level precision techniques are expected to lay the groundwork for high-stability resonant MEMS sensors. In addition, stress-balanced thin-film deposition is essential for maintaining the designed resonance frequency and mode symmetry[204,205]. The addition of metal or dielectric layers alters the stiffness and effective mass of MEMS structures, while residual stresses accumulated during deposition can further shift the resonance depending on whether they are tensile or compressive. Hence, achieving a balanced stress profile across the wafer minimizes warpage and curvature of the structural layer, ensuring consistent mechanical response and frequency stability among devices.

Finally, it is possible to develop an integrated MEMS sensor that can simultaneously measure both magnetic and electric fields. Such sensors are foreseen to find application in various industrial fields such as the nondestructive diagnosis of electric systems, biomedical devices, and autonomous driving based on its affordability, lightweight design, and high reliability.

Acknowledgements

This work was supported by the National Research Foundation of Korea (NRF) grant funded by the Korea government (MSIT) (Nos. RS-2023-00222166 and RS-2024-00457040).

Author contributions

D.K. and Y.J. contributed equally to this work. They conducted the literature review, drafted the manuscript, and prepared it for submission. J.K. provided supervision, offered critical revisions, and reviewed the final version of the manuscript. All authors have read and approved the submitted version.

Competing interests

The authors declare no competing interests.

Received: 26 August 2025 Revised: 26 October 2025 Accepted: 24 November 2025

References

1. Maluf, N. & Williams, K. *Introduction to Microelectromechanical Systems Engineering* (Artech House, 2004).
2. Senturia, S. D. *Microsystem Design* (Springer Science & Business Media, 2007).
3. Council, N. R. *Microelectromechanical Systems: Advanced Materials and Fabrication Methods* (National Academies Press, 1998).
4. Madou, M. J. *Fundamentals of Microfabrication: The Science of Miniaturization* (CRC Press, 2018).
5. Bell, D. J., Lu, T., Fleck, N. A. & Spearing, S. M. MEMS actuators and sensors: observations on their performance and selection for purpose. *J. Micromech. Microeng.* **15**, S153 (2005).
6. Holmström, S. T., Baran, U. & Urey, H. MEMS laser scanners: a review. *J. Microelectromechanical Syst.* **23**, 259–275 (2014).
7. Nielson, G. N. & Barbastathis, G. Dynamic pull-in of parallel-plate and torsional electrostatic MEMS actuators. *J. Microelectromechanical Syst.* **15**, 811–821 (2006).

8. Batra, R., Porfiri, M. & Spinello, D. Review of modeling electrostatically actuated microelectromechanical systems. *Smart Mater. Struct.* **16**, R23 (2007).
9. Chuang, W.-C., Lee, H.-L., Chang, P.-Z. & Hu, Y.-C. Review on the Modeling of Electrostatic MEMS. *Sensors* **10**, 6149–6171 (2010).
10. Hirano, T., Furuhata, T., Gabriel, K. J. & Fujita, H. Design, fabrication, and operation of submicron gap comb-drive microactuators. *J. Microelectromechanical Syst.* **1**, 52–59 (1992).
11. Legtenberg, R., Groeneveld, A. & Elwenspoek, M. Comb-drive actuators for large displacements. *J. Micromech. Microeng.* **6**, 320 (1996).
12. Yeh, R., Hollar, S. & Pister, K. S. Single mask, large force, and large displacement electrostatic linear inchworm motors. *J. Microelectromechanical Syst.* **11**, 330–336 (2002).
13. Tusset, A. M., Balthazar, J. M., Bassinello, D. G., Pontes, B. R. & Felix, J. L. P. Statements on chaos control designs, including a fractional order dynamical system, applied to a "MEMS" comb-drive actuator. *Nonlinear Dyn.* **69**, 1837–1857 (2012).
14. Lee, K. B. & Lee, K. B. *Principles of Microelectromechanical Systems* (Wiley Online Library, 2011).
15. Algamili, A. S. et al. A review of actuation and sensing mechanisms in MEMS-based sensor devices. *Nanoscale Res. Lett.* **16**, 1–21 (2021).
16. Younis, M. I. *MEMS Linear and Nonlinear Statics and Dynamics*, Vol. 20 (Springer Science & Business Media, 2011).
17. Hajjaj, A., Jaber, N., Ilyas, S., Alfosail, F. & Younis, M. I. Linear and nonlinear dynamics of micro and nano-resonators: review of recent advances. *Int. J. Non Linear Mech.* **119**, 103328 (2020).
18. Wang, D., Watkins, C. & Xie, H. MEMS mirrors for LiDAR: a review. *Micromachines* **11**, 456 (2020).
19. Mestrom, R., Fey, R., Van Beek, J., Phan, K. & Nijmeijer, H. Modelling the dynamics of a MEMS resonator: simulations and experiments. *Sens. Actuators A: Phys.* **142**, 306–315 (2008).
20. Frangi, A., Guerrieri, A., Carminati, R. & Mendicino, G. Parametric resonance in electrostatically actuated micromirrors. *IEEE Trans. Ind. Electron.* **64**, 1544–1551 (2016).
21. Zhang, W.-M., Meng, G. & Chen, D. Stability, nonlinearity and reliability of electrostatically actuated MEMS devices. *Sensors* **7**, 760–796 (2007).
22. Elshurafa, A. M. et al. Nonlinear dynamics of spring softening and hardening in folded-MEMS comb drive resonators. *J. Microelectromechanical Syst.* **20**, 943–958 (2011).
23. Izawa, T., Sasaki, T. & Hane, K. Scanning micro-mirror with an electrostatic spring for compensation of hard-spring nonlinearity. *Micromachines* **8**, 240 (2017).
24. Zhang, W.-M., Yan, H., Peng, Z.-K. & Meng, G. Electrostatic pull-in instability in MEMS/NEMS: A review. *Sens. Actuators A.* **214**, 187–218 (2014).
25. Williams, R. P., Vatankhah, E. & Hall, N. A. Multidegree-of-freedom state-space modeling of nonlinear pull-in dynamics of an electrostatic mems microphone. *J. Microelectromechanical Syst.* **31**, 589–598 (2022).
26. Younis, M. I. & Nayfeh, A. A study of the nonlinear response of a resonant microbeam to an electric actuation. *Nonlinear Dyn.* **31**, 91–117 (2003).
27. Zuo, P., Li, G., Xie, W. & Yeow, J. T. In *2015 34th Chinese Control Conference (CCC)*. 593-597 (IEEE). https://doi.org/10.23919/CCC58697.2023.10239917
28. Brunner, D., Yoo, H. W. & Schitter, G. Linear modeling and control of comb-actuated resonant MEMS mirror with nonlinear dynamics. *IEEE Trans. Ind. Electron.* **68**, 3315–3323 (2020).
29. Chu, Y., Fei, J. & Hou, S. Adaptive neural backstepping PID global sliding mode fuzzy control of MEMS gyroscope. *IEEE Access* **7**, 37918–37926 (2019).
30. Zhou, Y. et al. Design of force-to-rebalanced system with adaptive fuzzy-PID controller for N= 3 MEMS disk gyroscope. *IEEE Sens. J.* **21**, 13384–13393 (2021).
31. Rahmani, M. & Redkar, S. Data-driven Koopman fractional order PID control of a MEMS gyroscope using bat algorithm. *Neural Comput. Appl.* **35**, 9831–9840 (2023).
32. Xu, Z. et al. Intermittently dynamic fuzzy learning-based tracking control of amplitude signals for vibratory gyroscopes with composite identification. *IEEE Trans. Instrum. Measur.* **74**, 9518508 (2025).
33. Xu, Z., Wang, D., Yi, G. & Hu, Z. Asynchronous tracking control of amplitude signals in vibratory gyroscopes with partially unknown mode information. *IEEE Trans. Ind. Electron.* **70**, 7478–7487 (2022).
34. Borovic, B., Liu, A. Q., Popa, D., Cai, H. & Lewis, F. L. Open-loop versus closed-loop control of MEMS devices: choices and issues. *J. Micromech. Microeng.* **15**, 1917–1924 (2005).
35. Li, Q., Goosen, J. F. L., van Keulen, F. & van Beek, J. T. M. Gas Ambient Dependence of Quality factor in MEMS resonators. *IEEE Sens.* 1040, https://doi.org/10.1109/lcsens.2009.5398588 (2009).
36. Jiang, B., Huang, S., Zhang, J. & Su, Y. Analysis of frequency drift of silicon MEMS resonator with temperature. *Micromachines* **12**, https://doi.org/10.3390/mi12010026 (2020).
37. Schiwietz, D., Weig, E. M. & Degenfeld-Schonburg, P. Thermoelastic damping in MEMS gyroscopes at high frequencies. *Microsyst. Nanoeng.* **9**, 11 (2023).
38. Abdolvand, R., Bahreyni, B., Lee, J. E. & Nabki, F. Micromachined resonators: a review. *Micromachines* **7**, https://doi.org/10.3390/mi7090160 (2016).
39. Wang, Q., Xie, W., Xi, B., Sun, Y. & Yi, G. Rate integrating hemispherical resonator gyroscope detection error analysis and compensation. *IEEE Sens. J.* **23**, 7068–7076 (2023).
40. Xu, Z., Xi, B., Yi, G. & Ahn, C. K. High-precision control scheme for hemispherical resonator gyroscopes with application to aerospace navigation systems. *Aerosp. Sci. Technol.* **119**, https://doi.org/10.1016/j.ast.2021.107168 (2021).
41. Xu, Z., Yi, G. & Zhu, W. An accurate thermoelastic model and thermal output error analysis of a hemispherical resonator gyroscope under varying temperatures. *Mech. Syst. Sig. Process.* **170**, https://doi.org/10.1016/j.ymssp.2021.108760 (2022).
42. He, J., Zhou, W., He, X., Yu, H. & Ran, L. Drift of MEMS closed-loop accelerometers induced by dielectric charging. *IEEE Trans. Instrum. Meas.* **70**, 1–7 (2021).
43. Mahdavi, M., Ramezany, A., Kumar, V. & Pourkamali, S. In *2015 28th IEEE International Conference on Micro Electro Mechanical Systems (MEMS).* 913–916 (IEEE). https://doi.org/10.1109/MEMSYS.2015.7051108
44. Vig, J. R. & Kim, Y. Noise in microelectromechanical system resonators. *IEEE Trans. Ultrason. Ferroelectr. Frequency Control* **46**, 1558–1565 (1999).
45. Mohd-Yasin, F. & Nagel, D. J. Noise as diagnostic tool for quality and reliability of MEMS. *Sensors* **21**, 1510 (2021).
46. Qiao, Y., Arabi, M., Xu, W., Zhang, H. & Abdel-Rahman, E. M. The impact of thermal-noise on bifurcation MEMS sensors. *Mech. Syst. Signal Process.* **161**, 107941 (2021).
47. Leland, R. P. Mechanical-thermal noise in MEMS gyroscopes. *IEEE Sens. J.* **5**, 493–500 (2005).
48. Ali, G. & Mohd-Yasin, F. Noise in piezoelectric MEMS: a review. *IEEE Sens. J.* **25**, 16575–16592 (2025).
49. Mohammadi, A., Yuce, M. R. & Moheimani, S. O. in *IECON 2011-37th Annual Conference of the IEEE Industrial Electronics Society*. 4054–4058 (IEEE).
50. Mohammadi, A., Yuce, M. R. & Moheimani, S. R. A low-flicker-noise MEMS electrothermal displacement sensing technique. *J. Microelectromechanical Syst.* **21**, 1279–1281 (2012).
51. Schneider, M. & Schmid, U. In *MikroSystemTechnik Kongress 2023; Kongress.* 681–685 (VDE). http://hdl.handle.net/20.500.12708/192875
52. Fan, Z. et al. in *2024 IEEE SENSORS*. 1–4 (IEEE). https://doi.org/10.1109/SENSORS60989.2024.10784948
53. Wu, J., Fedder, G. K. & Carley, L. R. A low-noise low-offset capacitive sensing amplifier for a 50-/spl mu/g//spl radic/Hz monolithic CMOS MEMS accelerometer. *IEEE J. Solid State Circuits* **39**, 722–730 (2004).
54. Belousov, E., Timoshenko, A. & Lomovskaya, K. In *2016 IEEE NW Russia Young Researchers in Electrical and Electronic Engineering Conference (EIConRusNW)*. 495–498 (IEEE). https://doi.org/10.1109/EIConRusNW.2016.7448230
55. Xu, Z., Xi, B., Yi, G. & Wang, D. A novel model for fully closed-loop system of hemispherical resonator gyroscope under force-to-rebalance mode. *IEEE Trans. Instrum. Meas.* **69**, 9918–9930 (2020).
56. Demir, A. Understanding fundamental trade-offs in nanomechanical resonant sensors. *J. Appl. Phys.* **129**, 044503 (2021).
57. Sapsanis, C., Sophocleous, M., Andreou, A. G. & Georgiou, J. Trade-offs in sensor systems design: A tutorial. *IEEE Sens. J.* **22**, 10040–10061 (2022).
58. Verreault, A., Cicek, P.-V. & Robichaud, A. Oversampling ADC: a review of recent design trends. *IEEE Access* **12**, 121753–121779 (2024).
59. Lenz, J. & Edelstein, S. Magnetic sensors and their applications. *IEEE Sens. J.* **6**, 631–649 (2006).
60. Diaz-Michelena, M. Small magnetic sensors for space applications. *Sensors* **9**, 2271–2288 (2009).
61. Ripka, P. & Janosek, M. Advances in magnetic field sensors. *IEEE Sens. J.* **10**, 1108–1116 (2010).
62. Tumanski, S. Modern magnetic field sensors–a review. *Organ* **10**, 1–12 (2013).
63. Yin, X., Jiao, Q., Yuan, L. & Liou, S.-H. MEMS torsion oscillator magnetic field sensor. *IEEE T Magn.* **49**, 3890–3892 (2013).

64. Herrera-May, A. L., Aguilera-Cortes, L. A., Garcia-Ramirez, P. J. & Manjarrez, E. Resonant magnetic field sensors based on MEMS technology. *Sensors* **9**, 7785–7813 (2009).
65. Herrera-May, A. L. et al. Recent advances of MEMS resonators for Lorentz force based magnetic field sensors: design, applications and challenges. *Sensors* **16**, https://doi.org/10.3390/s16091359 (2016).
66. Dias, R. A. et al. in *2020 IEEE 33rd International Conference on Micro Electro Mechanical Systems (MEMS)*. 873–876. https://doi.org/10.1109/MEMS46641.2020.9056126
67. Ghosh, S. & Lee, J. E. Y. A piezoelectric-on-silicon width-extensional mode Lorentz force resonant MEMS magnetometer. *Sens. Actuators A* **260**, 169–177 (2017).
68. Ghosh, S. & Lee, J. E. Y. Extended bandwidth piezoelectric Lorentz force magnetometer based on a mechanically coupled beam resonator array. *IEEE T Magn.* **54**, 1–7 (2018).
69. Ghosh, S. & Lee, J. E. Y. Piezoelectric-on-silicon Lorentz force magnetometers based on radial contour mode disk resonators. *Sens. Actuators A* **281**, 185–195 (2018).
70. Shao, S., Gao, A., Wang, Y. & Wu, T. In *2021 IEEE 34th International Conference on Micro Electro Mechanical Systems (MEMS)*. 879–882 (IEEE). https://doi.org/10.1109/MEMS51782.2021.9375335
71. Tang, K.-W., Cheng, P.-C., Trivedi, S. & Li, S.-S. In *2021 21st International Conference on Solid-State Sensors, Actuators and Microsystems (Transducers)*. 414–417 (IEEE). https://doi.org/10.1109/Transducers50396.2021.9495675
72. Aditi & Gopal, R. Fabrication of MEMS xylophone magnetometer by anodic bonding technique using SOI wafer. *Microsyst. Technol.* **23**, 81–90, https://doi.org/10.1007/s00542-016-2812-8 (2016).
73. Alvarado-Rosas, V. O., Herrera-May, A. L. & Aguilera-Cortés, L. A. Mechanical design of a novel MEMS resonant sensor for monitoring in-plane magnetic fields. *Microsyst. Technol.* **23**, 3245–3255 (2016).
74. Wu, L., Tian, Z., Ren, D. & You, Z. A miniature resonant and torsional magnetometer based on Lorentz force. *Micromachines* **9**, https://doi.org/10.3390/mi9120666 (2018).
75. Kumar, V., Ramezany, A., Mahdavi, M. & Pourkamali, S. Amplitude modulated Lorentz force MEMS magnetometer with picotesla sensitivity. *J. Micromech. Microeng* **26**, 105021 (2016).
76. Ding, J. et al. A resonant microcantilever sensor for in-plane multi-axis magnetic field measurements. *J. Micromech. Microeng.* **29**, https://doi.org/10.1088/1361-6439/ab18ed (2019).
77. Al-Mahdi, O. L. Q., Ahmed, A., Dennis, J. & Khir, M. M. In *2020 8th International Conference on Intelligent and Advanced Systems (ICIAS)*. 1–4 (IEEE). https://doi.org/10.1109/ICIAS49414.2021.9642619
78. Du, H., Zhou, G., Zhao, Y., Chen, G. & Chau, F. S. Magnetic field sensor based on coupled photonic crystal nanobeam cavities. *Appl. Phys. Lett.* **110**, https://doi.org/10.1063/1.4975804 (2017).
79. Park, S., Al-Ghamdi, M. S., Khater, M. E. & Abdel-Rahman, E. A tunable MEMS magnetic sensor. *J. Microelectromechanical Syst.* **26**, 255–263 (2017).
80. Acevedo-Mijangos, J. et al. Design and fabrication of a microelectromechanical system resonator based on two orthogonal silicon beams with integrated mirror for monitoring in-plane magnetic field. *Adv. Mech. Eng.* **11**, 1687814019853683 (2019).
81. Alcheikh, N. & Younis, M. I. Resonator-based bidirectional Lorentz force magnetic sensor. *IEEE Electron Device Lett.* **42**, 406–409 (2021).
82. Li, M., Nitzan, S. & Horsley, D. A. Frequency-modulated Lorentz force magnetometer with enhanced sensitivity via mechanical amplification. *IEEE Electron Device Lett.* **36**, 62–64 (2015).
83. Sonmezoglu, S. et al. in *2017 IEEE International Symposium on Inertial Sensors and Systems (INERTIAL)*. 160–163.
84. Chen, F., Zhou, W., Zou, H., Kraft, M. & Li, X. in *2018 IEEE Micro Electro Mechanical Systems (MEMS)*. 940–943.
85. Sanchez-Chiva, J. M., Valle, J., Fernandez, D. & Madrenas, J. A mixed-signal control system for Lorentz-force resonant MEMS magnetometers. *IEEE Sens. J.* **19**, 7479–7488 (2019).
86. Li, M., Sonmezoglu, S. & Horsley, D. A. Extended bandwidth Lorentz force magnetometer based on quadrature frequency modulation. *J. Microelectromechanical Syst.* **24**, 333–342 (2015).
87. Liu, S., Xu, H., Xu, D. & Xiong, B. Modelling of resonant MEMS magnetic field sensor with electromagnetic induction sensing. *Solid State Electron.* **132**, 91–98 (2017).
88. Liu, S., Liang, H. & Xiong, B. An out-of-plane electromagnetic induction based resonant MEMS magnetometer. *Sens. Actuators A.* **285**, 248–257 (2019).
89. Wu, G., Xu, D., Xiong, B., Feng, D. & Wang, Y. Resonant magnetic field sensor with capacitive driving and electromagnetic induction sensing. *IEEE Electron Device Lett.* **34**, 459–461 (2013).
90. Wu, G. Q., Xu, D. H., Xiong, B., Che, L. F. & Wang, Y. L. Design, fabrication and characterization of a resonant magnetic field sensor based on mechanically coupled dual-microresonator. *Sens. Actuators A* **248**, 1–5 (2016).
91. Zhang, W. & Lee, J. E. In *2014 European Frequency and Time Forum (EFTF)*. 24–27. https://doi.org/10.1109/EFTF.2014.7331417
92. Liu, S., Liang, H. & Xiong, B. In *2019* 20th *International* Conference *on Solid-State Sensors, Actuators and Microsystems* & Eurosensors XXXIII (TRANSDUCERS & EUROSENSORS XXXIII). 138–141 (IEEE). https://doi.org/10.1109/TRANSDUCERS.2019.8808475
93. Liang, H., Liu, S. & Xiong, B. In-plane-sense magnetometer based on torsional MEMS with vertically-interlaced combs via self-alignment technique. *IEEE Electron Device Lett.* **41**, 900–903 (2020).
94. Liang, H., Liu, S. & Xiong, B. In *2020 IEEE 33rd International Conference on Micro Electro Mechanical Systems (MEMS)*. 1171–1174. https://doi.org/10.1109/MEMS46641.2020.9056214
95. Jung, Y., Jo, E. & Kim, J. Electrostatically driven two-axis microelectromechanical magnetometer with eccentric resonator and electromagnetic inductor. *Sens. Actuators A* **387**, 116378 (2025).
96. Jandakl, M., Vaqner, M. & Neuzil, T. In *2018 DGON Inertial Sensors and Systems (ISS)*. 1–14 (IEEE). https://doi.org/10.1109/InertialSensors.2018.8577156
97. Guo, Q. et al. Personal inertial navigation system assisted by MEMS ground reaction sensor array and interface ASIC for GPS-denied environment. *IEEE J. Solid State Circ.* **53**, 3039–3049 (2018).
98. Bao, S. D., Meng, X. L., Xiao, W. & Zhang, Z. Q. Fusion of inertial/magnetic sensor measurements and map information for pedestrian tracking. *Sensors* **17**, https://doi.org/10.3390/s17020340 (2017).
99. Lou, L., Zhang, J., Xiong, Y. & Jin, Y. An improved roadside parking space occupancy detection method based on magnetic sensors and wireless signal strength. *Sensors* **19**, https://doi.org/10.3390/s19102348 (2019).
100. Zhu, H. & Yu, F. A vehicle parking detection method based on correlation of magnetic signals. *Int. J. Distributed Sens. Netw.* **11**, https://doi.org/10.1155/2015/361242 (2018).
101. Xu, X., Sun, Y., Tian, X. & Zhou, L. A novel joint angle estimation method for serial manipulator using MEMS sensors. *IEEE Trans. Ind. Electronics*, 1–1, https://doi.org/10.1109/tie.2019.2962442 (2020).
102. Fang, B., Sun, F., Liu, H. & Guo, D. A novel data glove using inertial and magnetic sensors for motion capture and robotic arm-hand teleoperation. *Ind. Robot. Int. J.* **44**, 155–165 (2017).
103. Han, H., Jang, H. & Yoon, S. W. In *2019 IEEE SENSORS. 1–4 (IEEE)*. https://doi.org/10.1109/SENSORS43011.2019.8956799
104. Zhu, K., Lee, W. K. & Pong, P. W. Non-contact capacitive-coupling-based and magnetic-field-sensing-assisted technique for monitoring voltage of overhead power transmission lines. *IEEE Sens. J.* **17**, 1069–1083 (2016).
105. Kainz, A. et al. Distortion-free measurement of electric field strength with a MEMS sensor. *Nat. Electron* **1**, 68–73 (2018).
106. Liyanage, S., Shafai, C., Chen, T. & Rajapakse, A. Torsional moving electric field sensor with modulated sensitivity and without reference ground. *Proceedings* **1**, https://doi.org/10.3390/proceedings1040350 (2017).
107. Roncin, A., Shafai, C. & Swatek, D. R. Electric field sensor using electrostatic force deflection of a micro-spring supported membrane. *Sens. Actuators A.* **123-124**, 179–184 (2005).
108. Chen, T., Shafai, C., Rajapakse, A., Liyanage, J. S. H. & Neusitzer, T. D. Micromachined ac/dc electric field sensor with modulated sensitivity. *Sens. Actuators A.* **245**, 76–84 (2016).
109. Williams, K. R., De Bruyker, D. P. H., Limb, S. J., Amendt, E. M. & Overland, D. A. Vacuum steered-electron electric-field sensor. *J. Microelectromechanical Syst.* **23**, 157–167 (2014).
110. Kobayashi, T., Oyama, S., Takahashi, M., Maeda, R. & Itoh, T. Microelectromechanical systems-based electrostatic field sensor using $Pb(Zr,Ti)O_3$ thin films. *Jpn. J. Appl. Phys.* **47**, 7533–7536 (2008).
111. Tao, C. in *2013 IEEE Power & Energy Society General Meeting*. 1–4.
112. Huang, J. a., Wu, X., Wang, X., Yan, X. & Lin, L. A novel high-sensitivity electrostatic biased electric field sensor. *J. Micromech. Microeng.* **25**, https://doi.org/10.1088/0960-1317/25/9/095008 (2015).
113. Zhang, J., Wang, Y., Chen, P., Lv, T. & Yu, H. AlScN-based quasi-static multi-degree-of-freedom piezoelectric mems micromirror with large mirror plate and high fill factor. *Sens. Actuat. A* **379**, 115868 (2024).

114. Hortschitz, W., Kainz, A., Beigelbeck, R., Schmid, G. & Keplinger, F. Review on sensors for electric fields near power transmission systems. *Measur. Sci. Technol.* **35**, https://doi.org/10.1088/1361-6501/ad243a (2024).
115. Barthod, C., Passard, M., Bouillot, J., Galez, C. & Farzaneh, M. High electric field measurement and ice detection using a safe probe near power installations. *Sens. Actuators A* **113**, 140–146 (2004).
116. Yang, P. et al. In *2011 16th International Solid-State Sensors, Actuators and Microsystems Conference* 1034–1037 (2011). https://doi.org/10.1109/TRANSDUCERS.2011.5969165
117. Maruvada, P. S., Dallaire, R. D. & Pedneault, R. Development of field-mill instruments for ground-level and above-ground electric field measurement under HVDC transmission lines. *IEEE Trans. Power Appar. Syst.* **PAS-102**, 738–744 (1983).
118. Tant, P. et al. Design and application of a field mill as a high-voltage DC meter. *IEEE Trans. Instrum. Meas.* **56**, 1459–1464 (2007).
119. Bahreyni, B., Wijeweera, G., Shafai, C. & Rajapakse, A. Analysis and design of a micromachined electric-field sensor. *J. Microelectromechanical Syst.* **17**, 31–36 (2008).
120. Wijeweera, G., Bahreyni, B., Shafai, C., Rajapakse, A. & Swatek, D. R. Micromachined electric-field sensor to measure AC and DC fields in power systems. *IEEE Trans. Power Deliv.* **24**, 988–995 (2009).
121. Chen, T., Shafai, C., Rajapakse, A. & Park, B. Y. Micromachined electric field mill employing a vertical moving shutter. *Proc. Eng.* **87**, 452–455 (2014).
122. Afsharipour, E. et al. Study of the shielding effect of a vertical moving shutter micromachined field mill for measuring dc electric field. *Measur. Sci. Technol.* https://doi.org/10.1088/1361-6501/ab9459 (2020).
123. Ghionea, S. et al. In *SENSORS, 2013 IEEE*. 1–4. https://doi.org/10.1109/ICSENS.2013.6688131
124. Horenstein, M. N. & Stone, P. R. A micro-aperture electrostatic field mill based on MEMS technology. *J. Electrost.* **51-52**, 515–521 (2001).
125. Gong, C., Xia, S., Deng, K., Bai, Q. & Chen, S. Electric field sensors based on MEMS technology. *J. Electron.* **22**, 443–448 (2005).
126. Peng, C. et al. Design and testing of a micromechanical resonant electrostatic field sensor. *J. Micromech. Microeng.* **16**, 914–919 (2006).
127. Denison, T. A., Shafran, J. S., Kuang, J. & Lundberg, K. H. In *2007 IEEE Instrumentation & Measurement Technology Conference IMTC 2007*. 1–5. https://doi.org/10.1109/IMTC.2007.379381
128. Lee, J., Zhu, Y. & Seshia, A. Room temperature electrometry with SUB-10 electron charge resolution. *J. Micromech. Microeng.* **18**, https://doi.org/10.1088/0960-1317/18/2/025033 (2008).
129. Yong, Z., Lee, J. E. Y. & Seshia, A. A. A resonant micromachined electrostatic charge sensor. *IEEE Sens. J.* **8**, 1499–1505 (2008).
130. Peng, C., Yang, P., Zhang, H., Guo, X. & Xia, S. Design of a novel closed-loop SOI MEMS resonant electrostatic field sensor. *Proc. Eng.* **5**, 1482–1485 (2010).
131. Fang, Y., Peng, C., Yang, P., Fang, D. & Xia, S. Electric field and induced charges distribution model for MEMS strip-type sensing electrodes. *Microsyst. Technol.* **23**, 143–150 (2015).
132. Ma, Q., Huang, K., Yu, Z. & Wang, Z. A MEMS-based electric field sensor for measurement of high-voltage DC synthetic fields in air. *IEEE Sens. J.* **17**, 7866–7876 (2017).
133. Mou, Y. et al. Research on a novel MEMS sensor for spatial DC electric field measurements in an ion flows field. *Sensors* **18**, https://doi.org/10.3390/s18061740 (2018).
134. Yang, P., Wen, X., Chu, Z., Ni, X. & Peng, C. AC/DC fields demodulation methods of resonant electric field microsensor. *Micromachines* **11**, https://doi.org/10.3390/mi11050511 (2020).
135. Yang, P., Peng, C., Fang, D., Wen, X. & Xia, S. Design, fabrication and application of an SOI-based resonant electric field microsensor with coplanar comb-shaped electrodes. *J. Micromech. Microeng.* **23**, https://doi.org/10.1088/0960-1317/23/5/055002 (2013).
136. Chu, Z. et al. A high sensitivity electric field microsensor based on torsional resonance. *Sensors* **18**, https://doi.org/10.3390/s18010286 (2018).
137. Makihata, M., Matsushita, K. & Pisano, A. P. MEMS-based non-contact voltage sensor with multi-mode resonance shutter. *Sens. Actuators A.* **294**, 25–36 (2019).
138. Jung, Y., Jo, E. & Kim, J. in *2025 23rd International Conference on Solid-State Sensors, Actuators and Microsystems (Transducers)* 251–254 (2025).
139. Wang, Y. et al. A novel micro electric field sensor with X-Y dual axis sensitive differential structure. *Sens. Actuators A* **229**, 1–7 (2015).
140. Ling, B. et al. Single-chip 3D electric field microsensor. *Front. Mech. Eng.* **12**, 581–590 (2017).
141. Wen, X. et al. In *SENSORS, 2014 IEEE*. 582–585. https://doi.org/10.1109/ICSENS.2014.6985065
142. Li, B. et al. In *2016 IEEE SENSORS*. 1–3 (IEEE). https://doi.org/10.1109/ICSENS.2016.7808814
143. Cao, G., Xu, X. & Xu, D. Real-time calibration of magnetometers using the RLS/ML algorithm. *Sensors* **20**, https://doi.org/10.3390/s20020535 (2020).
144. Zhao, W., Li, Z., Zhang, H., Yuan, Y. & Zhao, Z. A decoupled calibration method based on the multi-output support vector regression algorithm for three-dimensional electric-field sensors. *Sensors* **21**, https://doi.org/10.3390/s21248196 (2021).
145. Ling, B. et al. Design, fabrication and characterization of a MEMS-based three-dimensional electric field sensor with low cross-axis coupling interference. *Sensors* **18**, https://doi.org/10.3390/s18030870 (2018).
146. Ling, B. et al. In *2019 20th International Conference on Solid-State Sensors, Actuators and Microsystems & Eurosensors XXXIII (TRANSDUCERS & EUROSENSORS XXXIII)*. 222–225. https://doi.org/10.1109/TRANSDUCERS.2019.8808343
147. Rabenimanana, T. et al. Mass sensor using mode localization in two weakly coupled MEMS cantilevers with different lengths: design and experimental model validation. *Sens. Actuators A Phys.* **295**, 643–652 (2019).
148. Yang, J., Zhong, J. & Chang, H. A closed-loop mode-localized accelerometer. *J. Microelectromechanical Syst.* **27**, 210–217 (2018).
149. Hao, Y. et al. A mode-localized DC electric field sensor. *Sens. Actuat. A* **333**, https://doi.org/10.1016/j.sna.2021.113244 (2022).
150. Riehl, P. S., Scott, K. L., Muller, R. S., Howe, R. T. & Yasaitis, J. A. Electrostatic charge and field sensors based on micromechanical resonators. *J. Microelectromech. Syst.* **12**, 577–589 (2003).
151. Källstrand, B. et al. Measurements of high voltage DC fields in air. *IEEE Electr. Insulation Mag.* **33**, 24–34 (2017).
152. Lei, X. et al. Study of non-contact voltage detector of 1000kV UHV AC based on MEMS electric field sensor. *MATEC Web Conf.* **160**, https://doi.org/10.1051/matecconf/201816002001 (2018).
153. Tang, G. Research on the adjacent charged object monitoring device based on MEMS electric field sensing technology. *IOP Conf. Ser.* **382**, 042047 (2018).
154. Gebrial, W., Prance, R. J., Harland, C. J. & Clark, T. D. Noninvasive imaging using an array of electric potential sensors. *Rev. Sci. Instrum.* **77**, https://doi.org/10.1063/1.2213219 (2006).
155. Prance, R. J. & Aydin, A. Acquisition of a nuclear magnetic resonance signal using an electric field detection technique. *Appl. Phys. Lett.* **91**, https://doi.org/10.1063/1.2762276 (2007).
156. Harland, C., Clark, T. & Prance, R. Electric potential probes-new directions in the remote sensing of the human body. *Meas. Sci. Technol.* **13**, 163 (2001).
157. Merletti, R. & Hermens, H. Detection and conditioning of the surface EMG signal. *Electromyography* 107–131, https://doi.org/10.1002/0471678384.ch5 (2004).
158. Le Goc, M., Taylor, S., Izadi, S. & Keskin, C. In *Proceedings of the SIGCHI Conference on Human Factors in Computing Systems*. 3167–3170. https://doi.org/10.1145/2556288.2557331
159. Zhang, L., Chen, X., Li, P., Wang, C. & Li, M. A method for measuring the height of hand movements based on a planar array of electrostatic induction electrodes. *Sensors* **20**, https://doi.org/10.3390/s20102943 (2020).
160. Zou, C., Qin, Y., Sun, C., Li, W. & Chen, W. Motion artifact removal based on periodical property for ECG monitoring with wearable systems. *Pervasive Mob. Comput.* **40**, 267–278 (2017).
161. Muhammad Sayem, A. S., Hon Teay, S., Shahariar, H., Fink, P. L. & Albarbar, A. Review on smart electro-clothing systems (SeCSs). *Sensors* **20**, https://doi.org/10.3390/s20030587 (2020).
162. Bourier, F. et al. Accuracy assessment of catheter guidance technology in electrophysiology procedures: a comparison of a new 3D-based fluoroscopy navigation system to current electroanatomic mapping systems. *J. Cardiovasc Electrophysiol.* **25**, 74–83 (2014).
163. Bisignani, A., De Bonis, S., Mancuso, L., Ceravolo, G. & Bisignani, G. Implantable loop recorder in clinical practice. *J. Arrhythm.* **35**, 25–32 (2019).
164. Giancaterino, S., Lupercio, F., Nishimura, M. & Hsu, J. C. Current and future use of insertable cardiac monitors. *JACC Clin. Electrophysiol.* **4**, 1383–1396 (2018).
165. Gabriel, C., Gabriel, S. & Corthout, E. The dielectric properties of biological tissues .1. *Lit. Surv. Phys. Med. Biol.* **41**, 2231–2249 (1996).
166. Khalili, M., GholamHosseini, H., Lowe, A. & Kuo, M. M. Y. Motion artifacts in capacitive ECG monitoring systems: a review of existing models and reduction techniques. *Med Biol. Eng. Comput* **62**, 3599–3622 (2024).

167. Ahn, S. H., Jeong, J. & Kim, S. J. Emerging encapsulation technologies for long-term reliability of microfabricated implantable devices. *Micromachines* **10**, https://doi.org/10.3390/mi10080508 (2019).
168. Chi, Y. M., Jung, T. P. & Cauwenberghs, G. Dry-contact and noncontact biopotential electrodes: methodological review. *IEEE Rev. Biomed. Eng.* **3**, 106–119, https://doi.org/10.1109/RBME.2010.2084078 (2010).
169. Xie, X. et al. Long-term reliability of Al_2O_3 and Parylene C bilayer encapsulated Utah electrode array based neural interfaces for chronic implantation. *J. Neural Eng.* **11**, 026016 (2014).
170. Wu, Y. et al. Feedthrough effect in MEMS gyroscopes and fully differential feedthrough cancellation method. *Rev. Sci. Instrum.* **95**, https://doi.org/10.1063/5.0171793 (2024).
171. Chen, X. et al. Research on a feedthrough suppression scheme for MEMS gyroscopes based on mixed-frequency excitation signals. *Micromachines* **16**, https://doi.org/10.3390/mi16101120 (2025).
172. Spees, W. M. et al. Quantification and compensation of eddy-current-induced magnetic-field gradients. *J. Magn. Reson.* **212**, 116–123 (2011).
173. Zhang, W., Bu, J., Li, D., Zhang, K. & Zhou, M. Coupling interference between eddy current sensors for the radial displacement measurement of a cylindrical target. *Sensors* **22**, https://doi.org/10.3390/s22124375 (2022).
174. Yoo, Y. & Choi, B. D. Readout circuits for capacitive sensors. *Micromachines* **12**, https://doi.org/10.3390/mi12080960 (2021).
175. He, C. et al. Noise analysis and suppression methods for the front-end readout circuit of a microelectromechanical systems gyroscope. *Sensors* **24**, https://doi.org/10.3390/s24196283 (2024).
176. Trlep, M., Hamler, A., Jesenik, M. & Stumberger, B. Electric field distribution under transmission lines dependent on ground surface. *IEEE T Magn.* **45**, 1748–1751 (2009).
177. Liu, J. et al. Recurrence formula-based automatic gradient eddy current compensation method for a 0.255 T MRI system. *J. Magn. Reson* **380**, 107951 (2025).
178. Wu, B. et al. Proximity sensing electronic skin: principles, characteristics, and applications. *Adv. Sci.* **11**, e2308560 (2024).
179. Shin, B., Lee, J.-H., Yu, C., Kyung, H. & Lee, T. Magnetic field-based vehicle positioning system in long tunnel environment. *Appl. Sci.* **11**, https://doi.org/10.3390/app112411641 (2021).
180. Ishii, K. et al. Localization for autonomous vehicles using environmental magnetic field aided by magnetic markers. *Int. J. Intell. Transport. Syst. Res.* **23**, 733–746 (2025).
181. Kim, J., Park, B. J. & Kim, J. Empirical analysis of autonomous vehicle's lidar detection performance degradation for actual road driving in rain and fog. *Sensors* **23**, https://doi.org/10.3390/s23062972 (2023).
182. Mayton, B., LeGrand, L. & Smith, J. R. An electric field pretouch system for grasping and co-manipulation. *IEEE Int. Conf. Robot.*, 831–838, https://doi.org/10.1109/Robot.2010.5509658 (2010).
183. Mohamed, A. A. S., Shaier, A. A., Metwally, H. & Selem, S. I. Wireless charging technologies for electric vehicles: inductive, capacitive, and magnetic gear. *IET Power Electron.* **17**, 3139–3165 (2023).
184. Hentschel, U., Labitzke, F., Helwig, M., Winkler, A. & Modler, N. Aspects of foreign object detection in a wireless charging system for electric vehicles using passive inductive sensors. *World Electric Vehicle J.* **13**, https://doi.org/10.3390/wevj13120241 (2022).
185. Wang, Q., Li, X., Yang, F. & Gao, T. UAV-WPT system based on novel magnetic structure and model predictive control. *Sensors* **23**, https://doi.org/10.3390/s23156859 (2023).
186. Jawad, A. M. et al. Wireless drone charging station using class-E power amplifier in vertical alignment and lateral misalignment conditions. *Energies* **15**, https://doi.org/10.3390/en15041298 (2022).
187. Wang, Z. et al. A study on non-contact multi-sensor fusion online monitoring of circuit breaker contact resistance for operational state awareness. *Energies* **18**, https://doi.org/10.3390/en18102667 (2025).
188. Chen, K.-L. & Chen, H.-S. Implementation and feasibility of environmental electric field measurement based on unmanned aerial vehicle. *IEEE Trans. Power Deliv.* **39**, 1877–1888 (2024).
189. Rosner, D., Trifu, C., Tranca, C., Vasilescu, I. & Stancu, F. In *2018 17th RoEduNet Conference: Networking in Education and Research (RoEduNet)*. 1-5 (IEEE). https://doi.org/10.1109/ROEDUNET.2018.8514123
190. Rad, S. S. et al. Electromagnetic interference on unmanned aerial vehicles (UAVs): a case study of high power transmission line impacts. In *IEEE Transactions on Transportation Electrification* (IEEE, 2025).
191. Suo, C. et al. Research on UAV three-phase transmission line tracking and localization method based on electric field sensor array. *Sensors* **21**, 8400 (2021).
192. Novak III, V., Maalouf, J. & Shevde, S. Magnetic field navigation of unmanned autonomous vehicles. US patent 9975634 (2018).
193. Bastola, S. et al. Improved dipole source localization from simultaneous MEG-EEG data by combining a global optimization algorithm with a local parameter search: a brain phantom study. *Bioengineering* **11**, https://doi.org/10.3390/bioengineering11090897 (2024).
194. Seedat, Z. A. et al. Simultaneous whole-head electrophysiological recordings using EEG and OPM-MEG. *Imaging Neurosci (Camb)* **2**, https://doi.org/10.1162/imag_a_00179 (2024).
195. Peczalski, K. et al. Synchronous recording of magnetocardiographic and electrocardiographic signals. *Sci. Rep.* **14**, 4098 (2024).
196. Lin, W. Y. et al. Realization and technology acceptance test of a wearable cardiac health monitoring and early warning system with multichannel MCGs and ECG. *Sensors* **18**, https://doi.org/10.3390/s18103538 (2018).
197. Klotz, T., Gizzi, L. & Rohrle, O. Investigating the spatial resolution of EMG and MMG based on a systemic multi-scale model. *Biomech. Model Mechanobiol.* **21**, 983–997 (2022).
198. Yu, H., Gao, Y., Wu, H. & Ning, X. Synergistic voluntary muscle signal characteristic analysis and comparison of OPM-MMG and sEMG. *IEEE Trans. Instrum. Meas.* **74**, 1–16 (2025).
199. Xu, Z., Zhu, W., Yi, G. & Fan, W. Dynamic modeling and output error analysis of an imperfect hemispherical shell resonator. *J. Sound Vib.* **498**, 115964 (2021).
200. Xu, H. et al. Stability of capacitive MEMS oscillators. *Microsyst. Technol* **31**, 2169–2183 (2025).
201. Ding, Y. et al. In *2025 36th Annual SEMI Advanced Semiconductor Manufacturing Conference (ASMC)*. 1–4 (IEEE). https://doi.org/10.1109/ASMC64512.2025.11010638
202. Ren, D. et al. In *2013 Transducers & Eurosensors XXVII: The 17th International Conference on Solid-State Sensors, Actuators and Microsystems (TRANSDUCERS & EUROSENSORS XXVII)*. 462–465 (IEEE). https://doi.org/10.1109/Transducers.2013.6626803
203. Zaman, A., Guneroglu, U., Alsolami, A. & Wang, J. Piezoelectrically and capacitively transduced hybrid MEMS resonator with superior RF performance and enhanced parasitic mitigation by low-temperature batch fabrication. *Appl. Sci.* **14**, 8166 (2024).
204. Pandey, A. K., Venkatesh, K. & Pratap, R. Effect of metal coating and residual stress on the resonant frequency of MEMS resonators. *Sadhana* **34**, 651–661 (2009).
205. Dutta, S., Imran, M., Pal, R., Jain, K. & Chatterjee, R. Effect of residual stress on RF MEMS switch. *Microsyst. Technol.* **17**, 1739–1745 (2011).